

UNIVERSITY OF CALIFORNIA SAN DIEGO

The Topography of Neuronal Metabolism

A Thesis submitted in partial satisfaction of the requirements for the degree

Master of Science

in

Biology

by

Teva Wu Bracha

Committee in charge:

Professor Gulcin Pekkurnaz, Chair
Professor Stacey Glasgow
Professor Byungkook Lim

2019

The Thesis of Teva Wu Bracha is approved, and it is acceptable quality and form for publication of microfilm and electronically:

Chair

University of California San Diego

2019

TABLE OF CONTENTS

| | |
|--|-----|
| Signature Page..... | iii |
| Table of Contents..... | iv |
| List of Figures..... | v |
| Abstract of the Thesis..... | vi |
| I. Characterizing the localization of Phosphofructokinase-1 in neuronal cytoarchitecture | |
| Abstract..... | 2 |
| Introduction..... | 3 |
| Results..... | 8 |
| Discussion..... | 12 |
| Figures..... | 15 |
| Materials and Methods..... | 30 |
| II. Developing SHCellAnalyzer: a semi-automated platform for <i>in-situ</i> assessment of cellular bioenergetics | |
| Abstract..... | 36 |
| Introduction..... | 38 |
| Results..... | 41 |
| Discussion..... | 49 |
| Figures..... | 51 |
| Materials and Methods..... | 61 |
| Conclusion..... | 64 |
| References..... | 65 |

LIST OF FIGURES

| | |
|---|----|
| Figure 1.1: PFK and Mitochondria Coenrichment and Cotrafficking..... | 15 |
| Figure 1.2: TMG Treatment is insufficient to induce PFK clustering in mammalian cells | 17 |
| Figure 1.3: PFK Treatment with TMG Summary..... | 18 |
| Figure 1.4: TMG Treatment reduces PFK Fluorescent Signal..... | 19 |
| Figure 1.5: O-GlcNAcylation may redirect glucose flux through the Pentose Phosphate Pathway..... | 20 |
| Figure 1.6: PFK displays presynaptic localization independent of TTX or KCl treatment | 22 |
| Supplementary Figure 1.1: PFK Antibody Validation for Immunocytochemistry..... | 24 |
| Supplementary Figure 1.2: PFKM Antibody Validation for Western Blot..... | 26 |
| Supplementary Figure 1.3: Aldolase A Construct and Antibody Validation..... | 27 |
| Supplementary Figure 1.4: Comparison of KCl Treatment between Live and Fixed Cell Imaging..... | 28 |
| Figure 2.1: Metabolic Flux Assay Workflow..... | 51 |
| Figure 2.2: SHCellAnalyzer Workflow..... | 52 |
| Figure 2.3: Thresholding Algorithm Parameter Determination..... | 54 |
| Figure 2.4: Cell Size Cutoff (CSC) Parameter Determination | 55 |
| Figure 2.5: Region of Interest (ROI) Parameter Determination | 56 |
| Figure 2.6: Alignment Parameter Determination | 57 |
| Figure 2.7: Cell Size Cutoff Validation | 58 |
| Figure 2.8: Metabolic Flux Data for HEK293T cells and Neurons | 59 |

ABSTRACT OF THE THESIS

by

Teva Wu Bracha

Master of Science in Biology

University of California San Diego, 2019

Professor Gulcin Pekkurnaz, Chair

Maintaining homeostasis through energy metabolism is a crucial function all cells must perform. This is especially true in the context of the brain, where even acute perturbations in energy levels can result in permanent brain damage. Discussed here are two separate projects focused on improving the understanding of and ability to examine neuronal energy metabolism. The first chapter discuss the localization of the rate-limiting enzyme of glycolysis, phosphofructokinase-1, in mammalian neurons. Evidence is shown of enrichment between phosphofructokinase-1 and mitochondria, suggesting a potential spatial coupling between the processes of glycolysis and

oxidative phosphorylation. The second project discusses the development of a program to efficiently normalize metabolic flux data through cell counts without a dedicated cell counting instrument. Metabolic flux assays are a powerful tool to gain insight into the rates of glycolysis and oxidative phosphorylation change in response to different experimental conditions. However, variance in the plated cell density of each well demands normalization to obtain accurate results. The software developed, SHCellAnalyzer, is comprised of two individual programs, an imageJ macro which physically counts the cells and a python script which takes those cell counts and extrapolates them to represent the entire well. Together these programs efficiently and accurately produce cell count estimates which can consistently be used to normalize metabolic flux data.

I. Characterizing the localization of Phosphofructokinase-1 in neuronal cytoarchitecture

Abstract

Neurons require a constant supply of energy to support synaptic activity and maintain homeostasis. While it is known that most of this energy is supplied through glycolysis and mitochondria, it remains unclear how the metabolic players involved in these processes coordinate their activity in the context of complex neuronal architecture. Previous research has shown that glycolytic enzymes dynamically cluster into a metabolic complex in response to hypoxia in *C. elegans* and *S. cerevisiae*. However, the position of mitochondria relative to these glycolytic complexes has not yet been examined. The spatial localization of these enzymes and mitochondria was investigated by transfecting primary rat neurons with mitochondria markers and fluorescently tagged Phosphofructokinase (PFK). These neurons were then live-cell imaged revealing instances of mitochondria and PFK enriching the same areas of the cell and trafficking together. The localization of PFK was similarly examined in the context of O-GlcNAcylation, a key regulatory post-translational modification upregulated in hypoxia, and neuronal depolarization. It was found that O-GlcNAcylation alone was insufficient to induce this dynamic clustering in mammalian neurons. Treatment with KCl to depolarize neurons seemed to cause PFK to become more punctate and associate with mitochondria at the synapse. However, this result was also seen with TTX treatment. It remains unclear what regulates the formation of the PFK clusters in hypoxic conditions and how these clusters associate with mitochondria. We provide some of the first evidence of the spatial association between mitochondria and in mammalian neurons and test how O-GlcNAcylation and neuronal activity affect their localization.

Introduction

Living organisms require energy to grow, reproduce, and function. Our bodies fight a constant tug-of-war between the production and expenditure of energy to maintain homeostasis. Though important throughout our bodies, energy regulation is exceptionally critical in the brain, where an energy deficit for even a few minutes can result in permanent damage [2]. The importance of energy in the brain is exemplified by the fact that it consumes 20% of our resting energy while accounting for only 2% of our total body mass [5]. Much research has gone into determining that synaptic transmission and synaptic vesicle recycling are responsible for the majority of the brain's energy consumption [2]. The regulation of energy generation with relation to synaptic activity is therefore key to understanding how our brains maintain energy homeostasis in response to a dynamically changing environment.

Two key metabolic processes produce most of the energy in our bodies: glycolysis and oxidative phosphorylation. The brain in particular utilizes glucose as its primary fuel source [5]. Glycolysis consists of the breakdown of glucose to pyruvate and is rapidly performed by a series of enzymes found in the cytoplasm. In contrast, oxidative phosphorylation takes place entirely within the mitochondria and converts pyruvate to water and carbon dioxide. These two processes are canonically considered coupled reactions, with glycolysis feeding directly into oxidative phosphorylation. To mediate this coupling, it seems likely that the glycolytic enzymes and mitochondria supporting these reactions are within close proximity in their subcellular localization. Yet, where these glycolytic enzymes and mitochondria are found in the cell with respect to each other remains unknown, especially in the context of neurons.

Due to their unique architecture of intricately branched dendrites and long axons, neurons face extra complications in maintaining energy homeostasis [6]. In humans, neurons can have individual processes that extend over a meter long and axons that may cover up to 4.5 meters total [8, 6]. Given the limited diffusion rate of ATP and massive size of neurons at the cellular level, there exists a clear need for locally produced energy in subcellular regions of the neuron [7]. Accordingly, determining the localization of mitochondria and glycolytic enzymes is critical to understanding how neurons meet their dynamic energy demands.

Mitochondria are not stationary organelles. They are constantly moving along microtubules and undergoing fusion and fission events with other mitochondria to support the energetic needs of the cell [6]. One of the processes that regulate mitochondrial motility and distribution is O-GlcNAcylation, a post-translational modification [1]. O-GlcNAcylation occurs in the cytoplasm and consists of the addition of a single GlcNAc moiety to specific serine and threonine residues of target proteins, similarly to phosphorylation. However, O-GlcNAc differs from phosphorylation in that there exists a single known protein that performs O-GlcNAcylation: O-GlcNAc Transferase (OGT). Similarly, O-GlcNAcase is the only known enzyme that can remove GlcNAc moieties from proteins [9]. These GlcNAc molecules are generated through the hexosamine biosynthetic pathway, a shunt of glycolysis. About 2-5% of glucose in glycolysis goes through the hexosamine pathway to become UDP-GlcNAc [10]. Accordingly, this signifies O-GlcNAcylation as a post-translational modification that is directly related to the levels of glucose in the body. Therefore, it has been hypothesized

that OGT and the process of O-GlcNAcylation mediates homeostasis by acting as a nutrient sensor [9].

Mitochondria move along microtubules through a protein complex called the mitochondria motor/adaptor complex [8]. This complex consists of Miro1, Milton, kinesin-1, and dynein. Mitochondria have been shown to preferentially localize to axonal branch points and presynaptic terminals to support the increased energy needs of these regions of the cell [6]. Mitochondria have also been shown to arrest in regions of high glucose via Milton O-GlcNAcylation [1]. However, as mitochondria themselves do not directly process glucose, the relative position of the glycolytic enzymes that do metabolize glucose comes into question.

Glycolytic enzymes are typically localized diffusely through the cytoplasm. However, it has been shown that in conditions of hypoxia, glycolytic enzymes dynamically coalesce to form distinct puncta in *C. elegans* and *S. cerevisiae* [3, 4]. In *C. elegans*, these clusters colocalized with presynaptic markers, indicating the formation of a glycolytic complex to support energy at the synapse [3]. These results were replicated using activity-dependent stimulation of neurons as well. However, no study has examined the formation of this glycolytic complex with respect to neighboring mitochondria, and the role of O-GlcNAcylation in the formation of these complexes. We hypothesize that mitochondria co-compartmentalizes with these glycolytic complexes and that O-GlcNAcylation plays a role in mediating this metabolic coupling.

One of the key players in this glycolytic complex is phosphofructokinase-1 (PFK), the rate-limiting enzyme of glycolysis. PFK forms a catalytically active tetramer, but can also be found as a less active dimer or monomer. In most mammals, PFK has three

isoforms primarily expressed in muscle (PFKM), liver (PFKL), or platelet (PFKP). The isoforms have approximately 70% sequence identity with each other, but aside from their differential tissue expression much of their functional differences remain unknown. One significant structural difference is that PFKL has been shown to form filaments composed of tetramers in vitro due to a difference in the isoform's regulatory domain [12]. It is unclear how the structure of PFK affects the formation of a glycolytic complex, but it is hypothesized that tetramer formation may be necessary for this phenomenon as well [13]. Additionally, PFK activity has been shown to be reduced via O-GlcNAcylation of a conserved serine residue [11]. There seems to be evidence that O-GlcNAcylation of PFK inhibits binding of fructose 2,6 bisphosphate to activate PFK and induce tetramerization [11]. However, hypoxia increases levels of O-GlcNAcylation and induces to O-GlcNAcylation of PFK [11]. How these contrasting pieces of evidence play a role in the metabolic coupling between glycolysis and mitochondria may be answered through the pentose phosphate pathway.

The pentose phosphate pathway (PPP) is a shunt of glycolysis in which glucose-6-phosphate is converted to gluconolactone rather than fructose-6-phosphate. The PPP generates many building blocks for the cell including lipids, nucleotides, and glutathione. Glutathione is of particular interest as it serves as an antioxidant to combat potentially harmful reactive oxygen species (ROS) generated through oxidative phosphorylation [14]. Previous studies have shown that the PPP is upregulated in cancer, likely to provide the building blocks needed for cell proliferation [14]. Interestingly, hypoxia and O-GlcNAcylation also increase flux through the PPP [11]. This may be due to the rate-limiting enzyme glucose-6-phosphate dehydrogenase (G6PD) activity being increased

via O-GlcNAcylation as well as PFK activity being decreased, diverting more glucose through the PPP. The questions of how glycolysis and PPP are regulated to maintain homeostasis in the context of neuronal architecture and what role O-GlcNAcylation plays in maintaining this balance remain unanswered.

We therefore seek to investigate the activity and localization of glycolytic enzymes relative to mitochondria and the synapse utilizing primary cultured rat neurons. This model allows for high resolution imaging and modulation of O-GlcNAcylation levels and synaptic activity to visualize the localization of glycolytic enzymes and mitochondria in differing metabolic states. Accordingly, we will be employing immunostaining, expression of tagged constructs, and live cell imaging to characterize the localization of glycolytic enzymes and mitochondria. We will modulate O-GlcNAcylation levels using TMG, an O-GlcNAcase inhibitor. As previous studies have shown the clustering of PFK into phase-separated bodies in hypoxic conditions, we hypothesize that increasing O-GlcNAcylation may recapitulate this clustering and that this glycolytic complex may compartmentalize with mitochondria to support the energy needs of neurons. We also treat neurons with TTX and KCl to broadly examine how activity changes the localization of these enzymes relative to the synapse and mitochondria in mammalian neurons.

Results

Evidence of PFK and Mitochondrial Co-trafficking

Ideally, an antibody to PFK would be used to investigate the enzyme's position relative to mitochondria. However, none of the antibodies we tested were deemed appropriate for immunostaining or western blot (SFig 1.1 and 1.2). We accordingly shifted our focus to overexpression constructs to investigate the dynamics of PFK relative to mitochondria. We transfected neurons on DIV10 with MitoDsRed, to label mitochondria, and eGFP-tagged PFKM, PFKM-eGFP. We then performed live-cell imaging on DIV13. The kymolyzer macro was used to generate kymographs of the images (Fig 1.1A). Areas of mitochondria and PFK enrichment were identified using peaks determined by the Find Peaks imageJ macro. The locations of these peaks were then compared to verify co-enrichment between mitochondrial and PFK signal (Fig 1.1C). Further investigation of these kymographs revealed instances of co-trafficking between mitochondria and PFK (Fig 1.1B). Plot profiles were made of the first and last frame of images showing a PFK peak that co-trafficked with a mitochondrion (Fig 1.1D). These results provided some of the first visual evidence of a conserved spatial dynamic interaction between mitochondria and PFK in mammalian neurons.

Globally Increasing O-GlcNAcylation Levels did not induce PFK clustering in Mammalian Neurons

We next decided to follow up on previous studies that have shown glycolytic enzymes form clusters in response to hypoxia in *C. elegans* and *S. cerevisiae* [3, 4]. We

hypothesized the increased O-GlcNAc levels found in hypoxia may be responsible for mediating this response. Accordingly, we repeated our transfection process, but treated our neurons overnight with TMG, an O-GlcNAcase inhibitor, the day before imaging. Comparing neurons treated with growth media versus TMG, we saw no difference in the localization of PFK (Fig 1.2A, B). Further examination of the plot profiles between the treatment conditions revealed no evidence of the dynamical clustering of PFKM in response to TMG treatment (Fig 1.2C, D).

We also wanted to examine whether increasing O-GlcNAcylation levels would impact the localization of PFK relative to mitochondria. We first evaluated mitochondria motility and the number of mitochondria per image to ensure PFK overexpression was not significantly perturb mitochondria motility. Though we saw no significant differences between control conditions and TMG treatment conditions, there was a clear trend towards decreased mitochondrial motility in neurons treated with TMG (Fig 1.3A, B). We then evaluated both the fraction of mitochondrial peaks overlapping with a PFK peak, the enrichment of PFK on mitochondria, and the fraction of PFK peaks overlapping with a mitochondrial peak, the enrichment of mitochondria on PFK (Fig 1.3C, D). For peak analysis, the images were first smoothed to reduce their noise and the overlapping peaks of mitochondria and PFK were found using the Find Peaks macro. A significant difference in the enrichment of PFK on mitochondria was determined by Kruskal-Wallis non-parametric test between GFP and PFKM-eGFP in control conditions. PFKM enriched mitochondria more frequently than GFP, supporting our previous findings suggesting a spatial preference between mitochondria and PFK. This trend was also seen with PFKL, but did not reach significance. Surprisingly, this trend disappeared with

TMG treatment, indicating the PFK's preference for mitochondria may actually decrease with O-GlcNAcylation. While imaging these neurons, we noticed a trend that PFKL-eGFP and PFKM-eGFP signals seemed fainter in neurons treated with TMG. We decided to quantify the mean fluorescence of the axons to investigate this phenomenon (Fig 1.4). Indeed, we see a consistent decrease in fluorescence in PFKL-eGFP and PFKM-eGFP, but not in regular GFP. This decrease in fluorescence specific to PFK could be indicative of either a change in protein degradation rate or trafficking.

These results made us reconsider the role of O-GlcNAcylation in the regulation of glucose metabolism. Previous studies have indicated that O-GlcNAcylation of PFK may decrease its activity causing glucose metabolism to favor the pentose phosphate pathway (PPP) [11]. This may be supported by the fact that O-GlcNAcylation of Glucose-6-Phosphate Dehydrogenase (G6PD) has been shown to increase its activity [16]. We consider the possibility that O-GlcNAcylation may increase glucose flux through the PPP as a shunt to increase overall glucose flux (Fig 1.5A). We utilized a G6PD activity assay kit to test previous findings that O-GlcNAcylation increases its activity. Our results indicate a modest increase of G6PD activity in response to increased O-GlcNAcylation levels (Fig 1.5B).

Glycolytic Enzymes Localize at Presynaptic Sites in Mammalian Neurons

Since we found that O-GlcNAcylation alone was insufficient to cluster PFK, we decided to investigate how neuronal activity would shape the distribution of PFK. We decided to use the blunt approach of KCl treatment to investigate how depolarization would shape PFK's distribution. Primary cortical neurons were transfected with

presynaptic marker vGlut1mCherry and either PFKL-eGFP or PFKM-eGFP. The cells were treated overnight with TTX and AP5 to silence activity two days after transfection and then either left in TTX or changed to media containing KCl. An hour after media change these neurons were fixed and stained for the mitochondrial marker Tomm20. Segments of axons treated with KCl were traced and evaluated for the colocalization between PFK, vGlut1, and Tomm20 (Fig 1.6A, B). We found regions containing overlapping peaks of all three channels (Fig 1.6C, D). We also quantified the percent of presynaptic terminals containing PFK (Fig 1.6E). Surprisingly, we found no significant difference between TTX and KCl treatments. There was some reduction of the enrichment of PFKL in TTX conditions, but not to a level of significance. However, these experiments need to be repeated to increase the sample size and independent replicates.

Discussion

Our findings provide the first pieces of evidence in establishing a spatial link between glycolytic enzymes and mitochondria in mammalian neurons. Specifically, we show evidence that PFK enriches and traffics with mitochondria in distal axonal regions. We see similar enrichment of PFK with presynaptic marker vGlut1. Recent findings have also shown that PFK is not evenly distributed in *C. elegans* neurons in normoxic conditions [13]. PFK signal appears initially higher in presynaptic compartments and indeed these PFK peaks predict the locations where hypoxia induced clusters will form. Alongside previous research indicating the enrichment of both glycolytic enzymes and mitochondria at the synapse, our findings suggest the formation of a presynaptic metabolic compartment to support the energy demands of neurotransmission and synaptic vesicle recycling. Follow-up experiments performing live-cell imaging in neurons with concurrently labeled mitochondria, PFK, and vGlut1 could assess the trafficking dynamics involved with the formation of this metabolic compartment at the synapse.

Though we see enrichment between mitochondria and PFK, we fail to see clear clusters as a result of increasing O-GlcNAcylation levels via TMG treatment. Previous studies showing the clustering of PFK were performed primarily in hypoxic conditions. Though O-GlcNAcylation is elevated in hypoxia, other factors altered during hypoxia may play a role in clustering PFK and other glycolytic enzymes. There is evidence that induced neuronal activity is sufficient to cluster PFK in *C. elegans*, suggesting that the clustering mechanism is likely intrinsically related to energy demand or stress rather than just hypoxia. We attempted to investigate the effects neuronal activity had on PFK

localization through TTX and KCl treatment, however our results showed no clear difference between PFK enrichment with presynaptic marker vGlut1 between conditions within our limited data set. Additionally, the enrichment of peaks seen with PFK was also present with GFP, indicating this enrichment may not be specific (SFig 1.4). We did not see clear clusters in live-cell images, but did see apparent clusters with a fixed-cell approach. It remains unclear whether the clusters we see with a fixed-cell approach are representative of the phenomenon as the clusters are present independent of TTX and KCl treatment. It is possible that through the fixation and washing process, the diffuse cytoplasmic pool of proteins are washed out leaving only more heavily clustered proteins during imaging. More investigation needs to be done to truly verify the dynamic clustering of glycolytic enzymes in mammalian neurons. A more specific method of neuronal stimulation using optogenetic techniques would allow for the imaging of PFK clustering dynamics based on activity in a temporally controlled manner. Alternatively, using chemogenetics with DREADDs would also allow for the temporal, control of neuronal activity to visualize and record these clustering dynamics. These experiments could better verify the formation and dynamics.

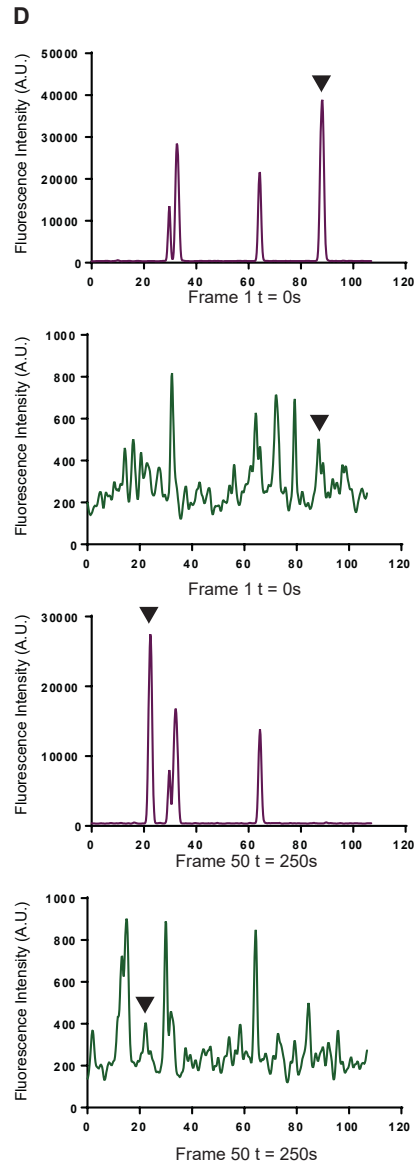
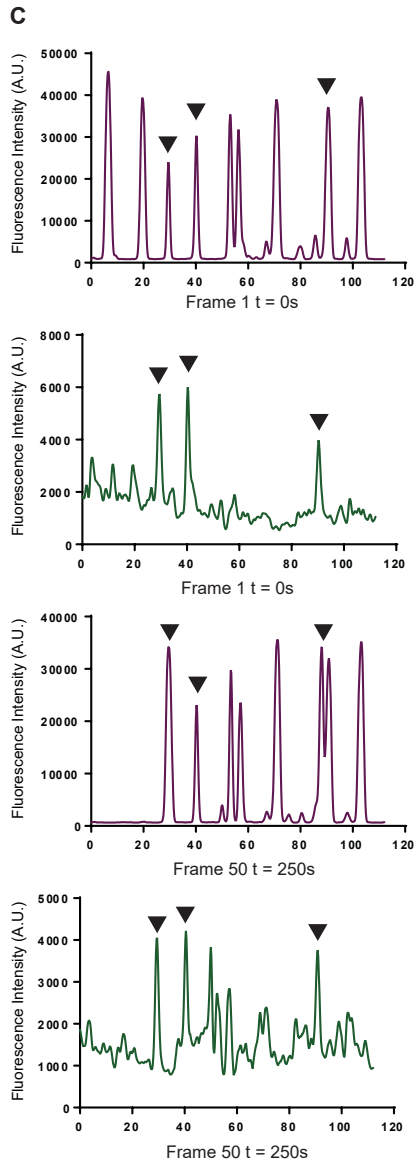
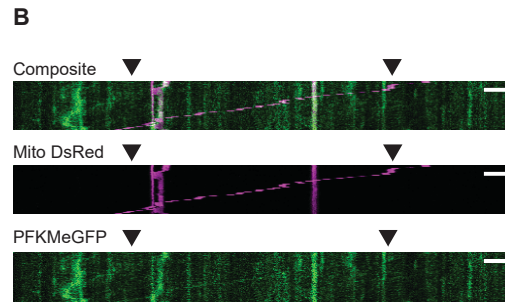
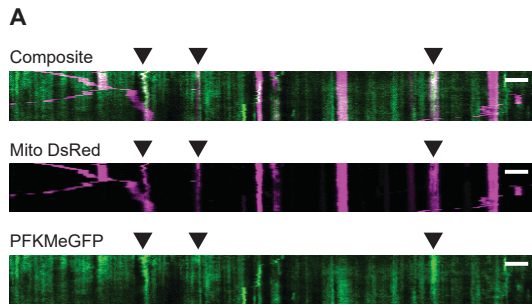
It is still unclear whether O-GlcNAcylation is actually increasing ATP production and glycolytic flux. Previous results have shown an apparent decrease in glycolytic activity in response to increased O-GlcNAcylation, but our lab has found the opposite effect on ATP production [11]. It seems consistent that increased O-GlcNAcylation at least increases the activity of G6PD and potentially flux through the PPP, but that still does not determine overall ATP production. The metabolites from the PPP can reenter glycolysis through the activity of transketolase and transaldolase. Metabolite tracing

would be the optimal way to fully address how O-GlcNAcylation redirects glucose flux and help evaluate whether O-GlcNAcylation is upregulating ATP generation.

The answer to these questions would lead to a significantly better understanding of how energy is dynamically regulated and generated in response to the changing needs of the environment. Understanding what key players are involved in the regulation of mitochondria and PFK finding each other in the unique space of neuronal processes would help evaluate what happens to these players in neurodegenerative diseases. Further research could be performed on local energy deficits caused by a lack of knowledge in how the key energy providers of the cell reach their target destinations. The work performed here provides some of the first evidence of a conserved interaction between mitochondria and PFK in mammalian cells.

Figures

Figure 1.1. PFK and Mitochondria Coenrichment and Cotrafficking. Time-lapse images of DIV13 cortical neurons transfected with MitoDsRed and PFKMeGFP. Kymographs show large coenrichment between PFK and Mitochondria (A) and instances of cotrafficking (B). Plot profiles from the first and last frame of these images reveal significant overlapping peaks between mitochondria (C) and a PFK peak that trafficked alongside mitochondria (D) indicated by black arrows. Scale bars represent 5 μ m.



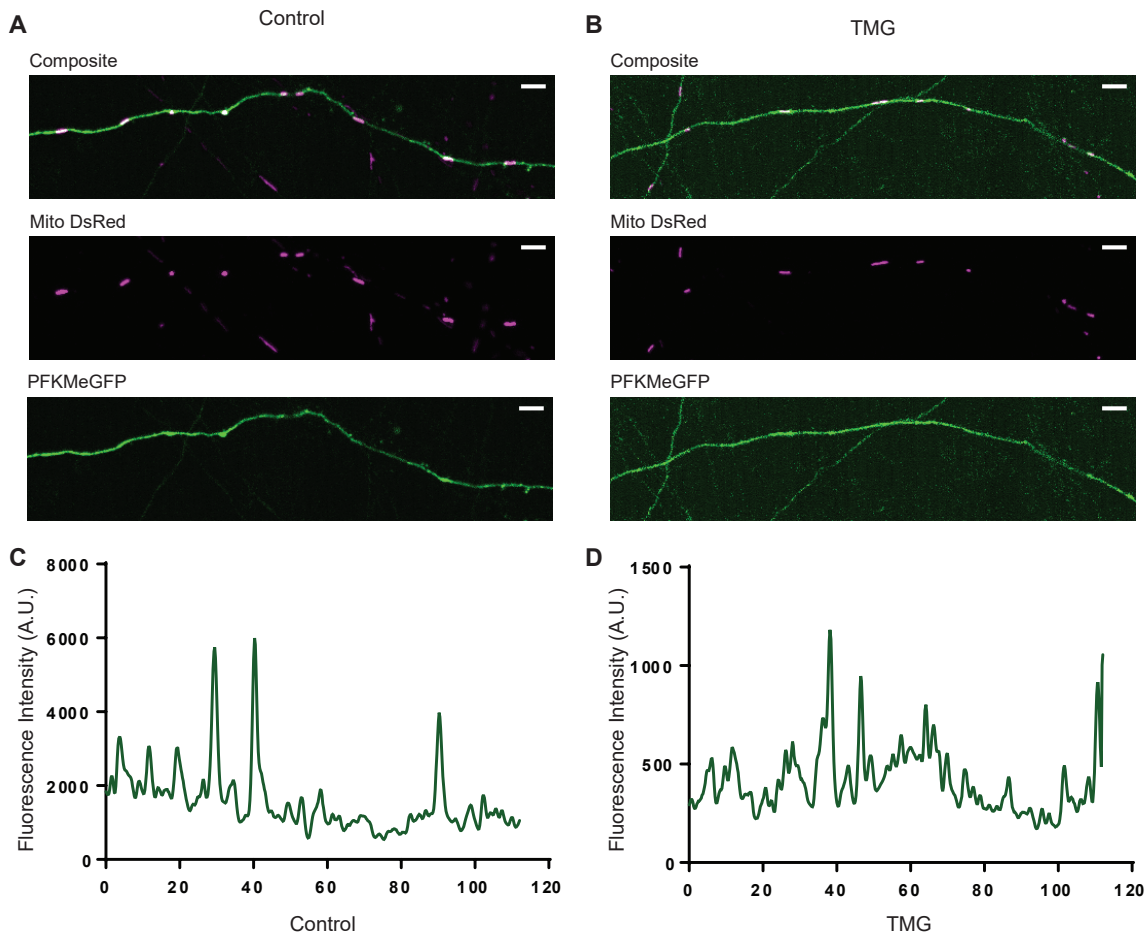


Figure 1.2. TMG Treatment is insufficient to induce PFK clustering in mammalian cells. Neurons transfected with MitoDsRed and PFKMeGFP were treated with either growth media (control) (A) or TMG (B). TMG treated neurons do not display clear distinct puncta in their distribution and do not appear overtly different from control neurons. Plot profiles from control (C) and TMG (D) neurons show no clear differences in distribution. Scale bars represent 5μm.

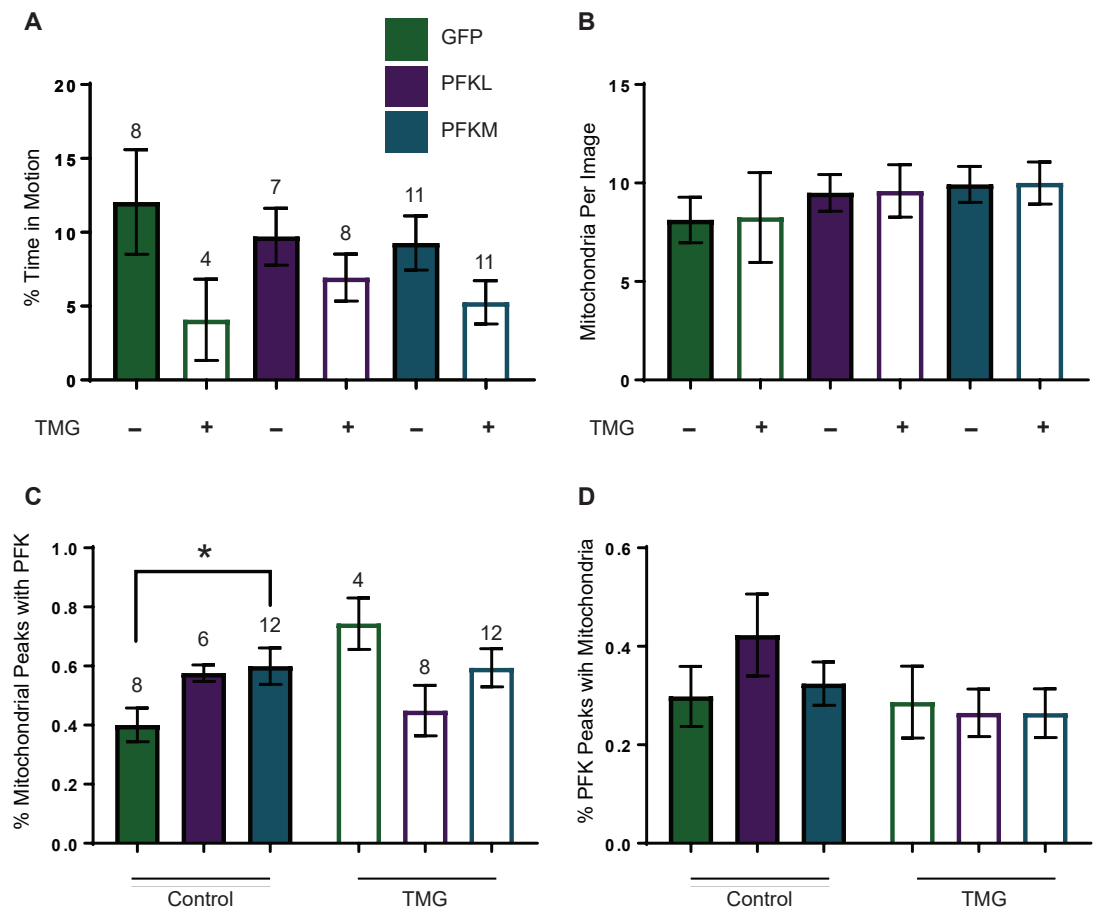


Figure 1.3. PFK Treatment with TMG Summary. Time-lapse images were taken of Neurons treated with either growth media (control) or TMG and transfected with MitoDsRed and either GFP, PFKLeGFP, or PFKMeGFP. Images were analyzed for percent time mitochondria in motion (A), mitochondria per image which displays 100-120um axons (B), percentage of mitochondrial peaks with an overlapping GFP channel peak (C), and percentage of GFP channel peaks with an overlapping mitochondrial peak (D). Percent time in motion and mitochondria per image were analyzed via Mann-Whitney test between TMG treatment conditions of neurons transfected with the same construct. No significant differences were found between groups, but some reduction in percent time in motion is seen in all groups treated with TMG as expected. Overlapping peaks were analyzed within TMG treatment groups by Kruskal-Wallis test. Unless indicated differences between groups did not reach a significant level of difference. Number of neurons analyzed is indicated on top of error bars. Sample size from (A) and (B) are conserved as well as (C) and (D). Neurons come from 2 to 3 independent preparations.

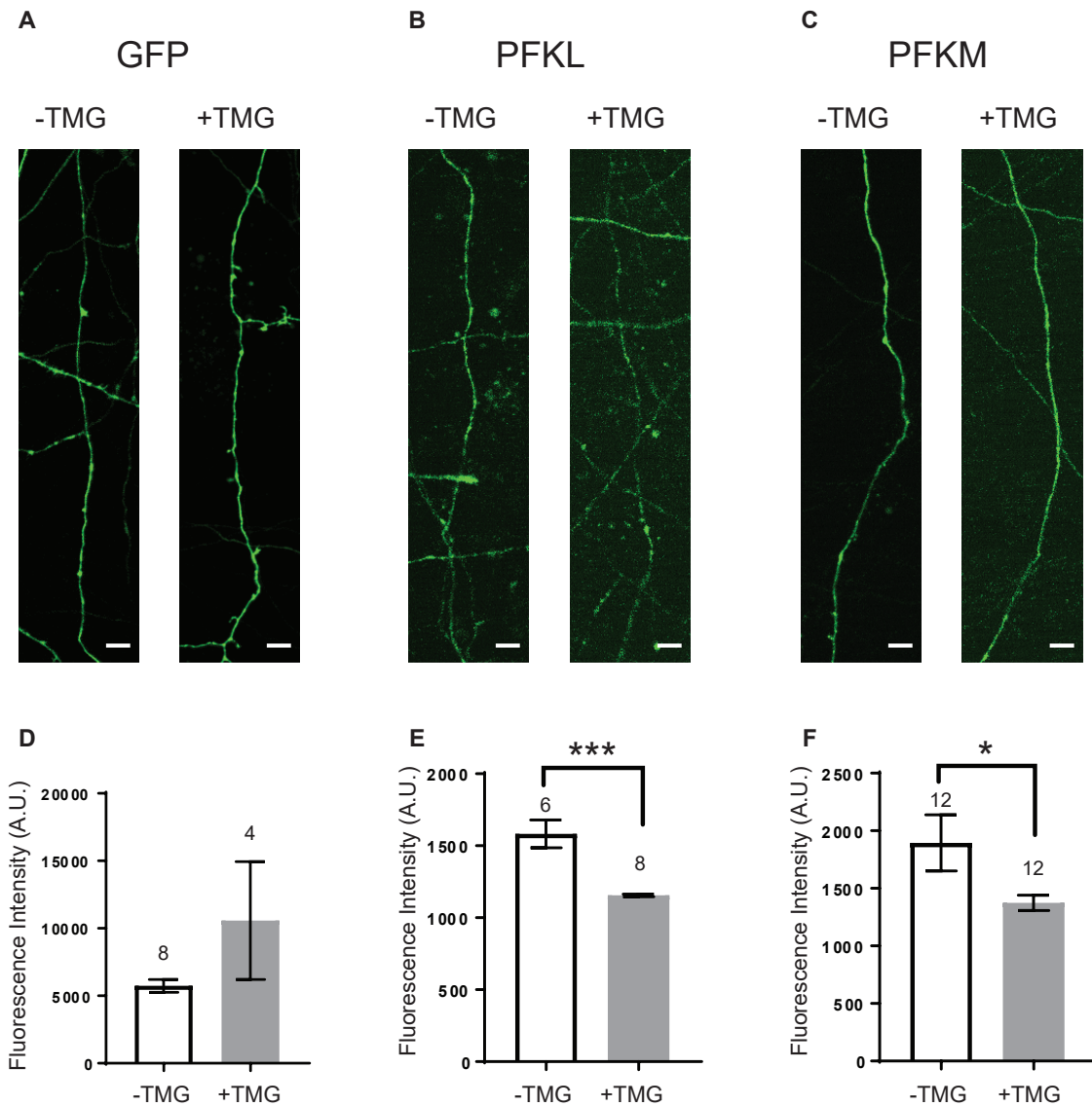


Figure 1.4. TMG Treatment reduces PFK Fluorescent Signal. Neurons expressing GFP (A), PFKLeGFP (B), or PFKMeGFP (C) and treated with either growth media (control) or TMG were time-lapse imaged. Axons were traced and the average fluorescent signal from the first and last frame of the images were quantified. No significant differences by t-test were found in GFP signal from TMG treatment (D), however both PFKL (E) and PFKM (F) showed significant decreases in fluorescent signal from TMG treatment. Number of measurements taken is indicated on top of error bars. Neurons come from 2 to 3 independent preparations. Scale bars represent 5 μ m.

Figure 1.5. O-GlcNAcylation may redirect glucose flux through the Pentose Phosphate Pathway. A schematic for glucose metabolism through both glycolysis and the pentose phosphate pathway is shown with predicted GlcNAc modulations (A). Inhibition of PFK may help increase overall flux through the pentose phosphate pathway. HEK293T cells mock transfected or transfected OGT and then treated with TMG were lysed and analyzed for G6PD activity (B). Data normalized through BCA assay and western blot (C).

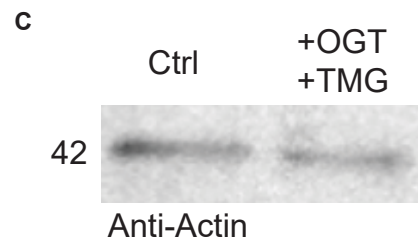
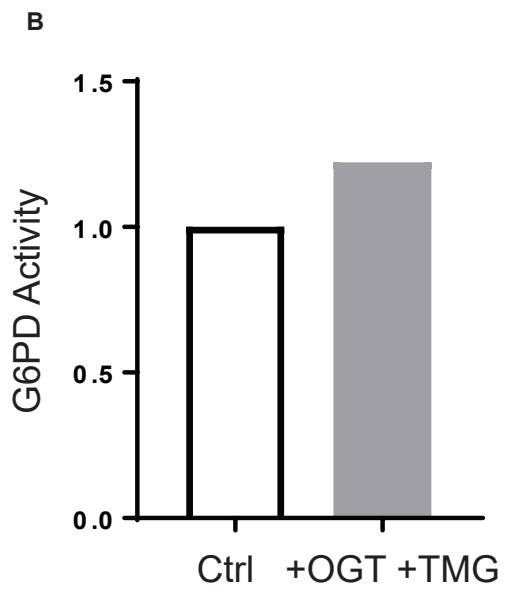
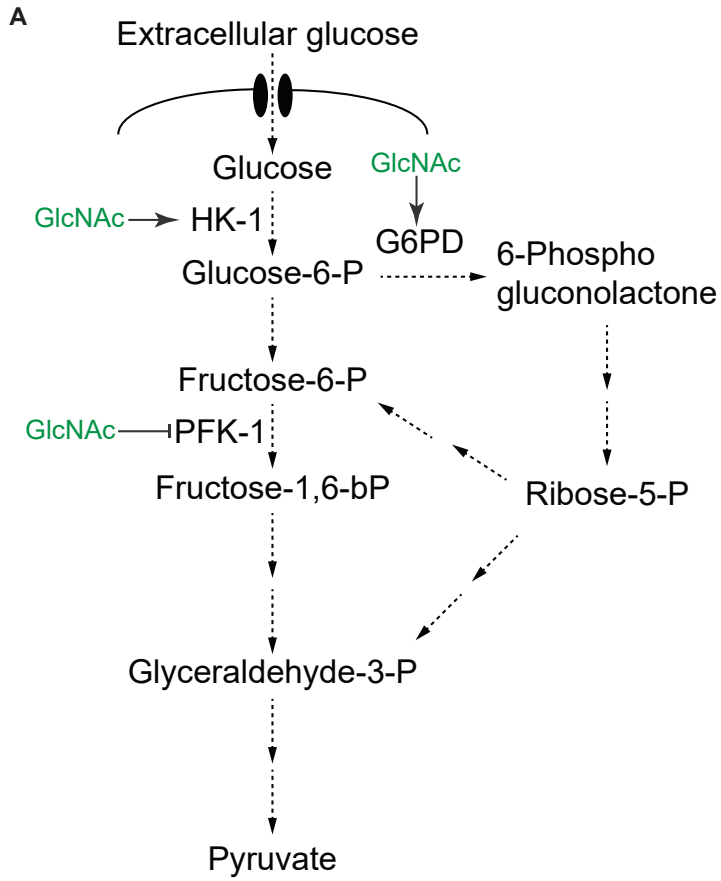
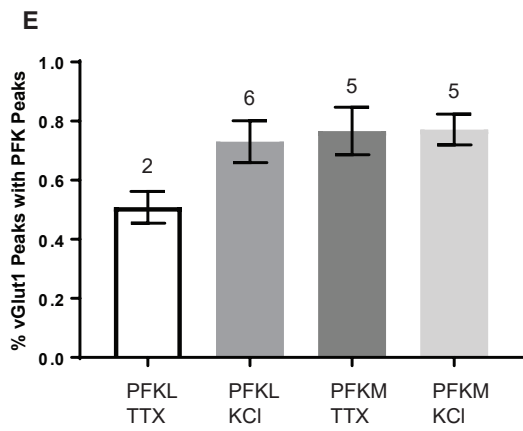
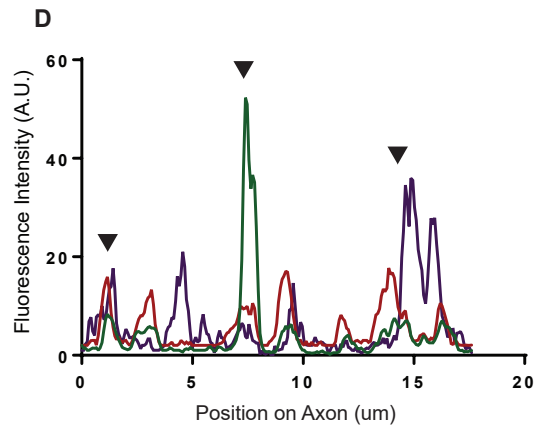
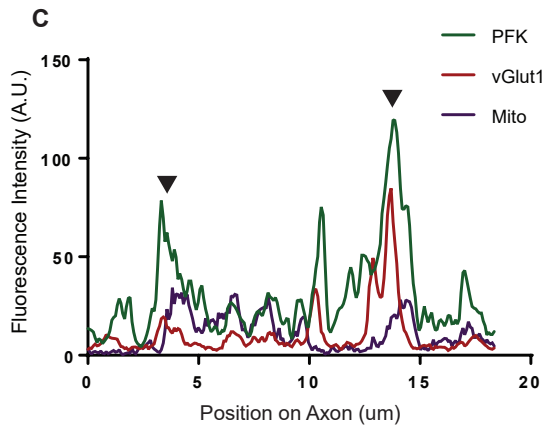
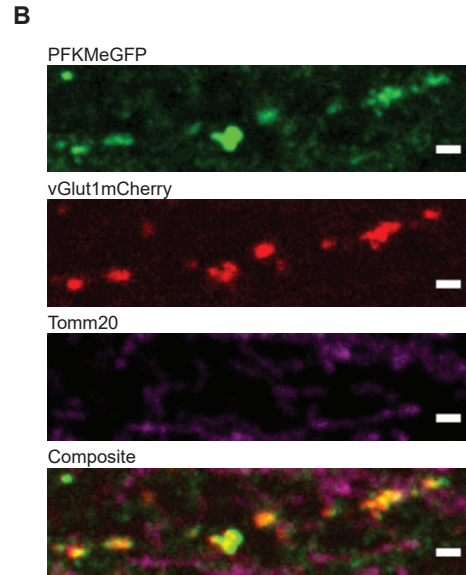
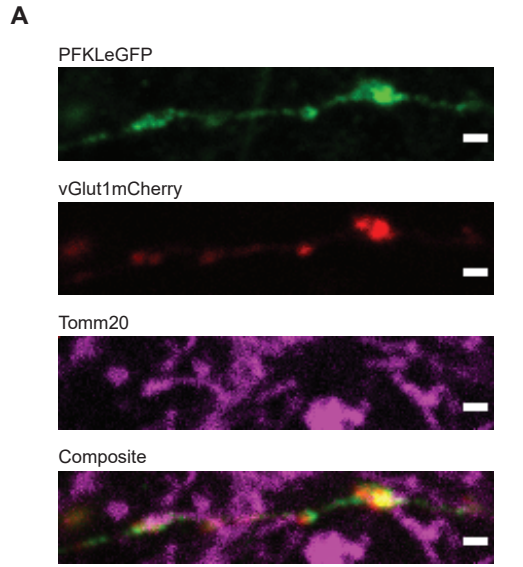
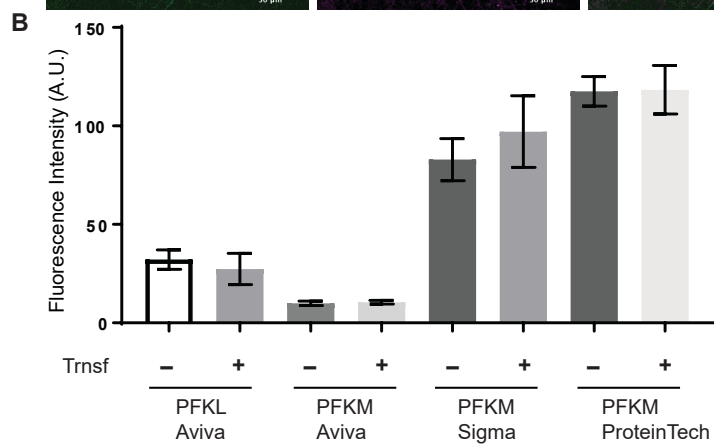
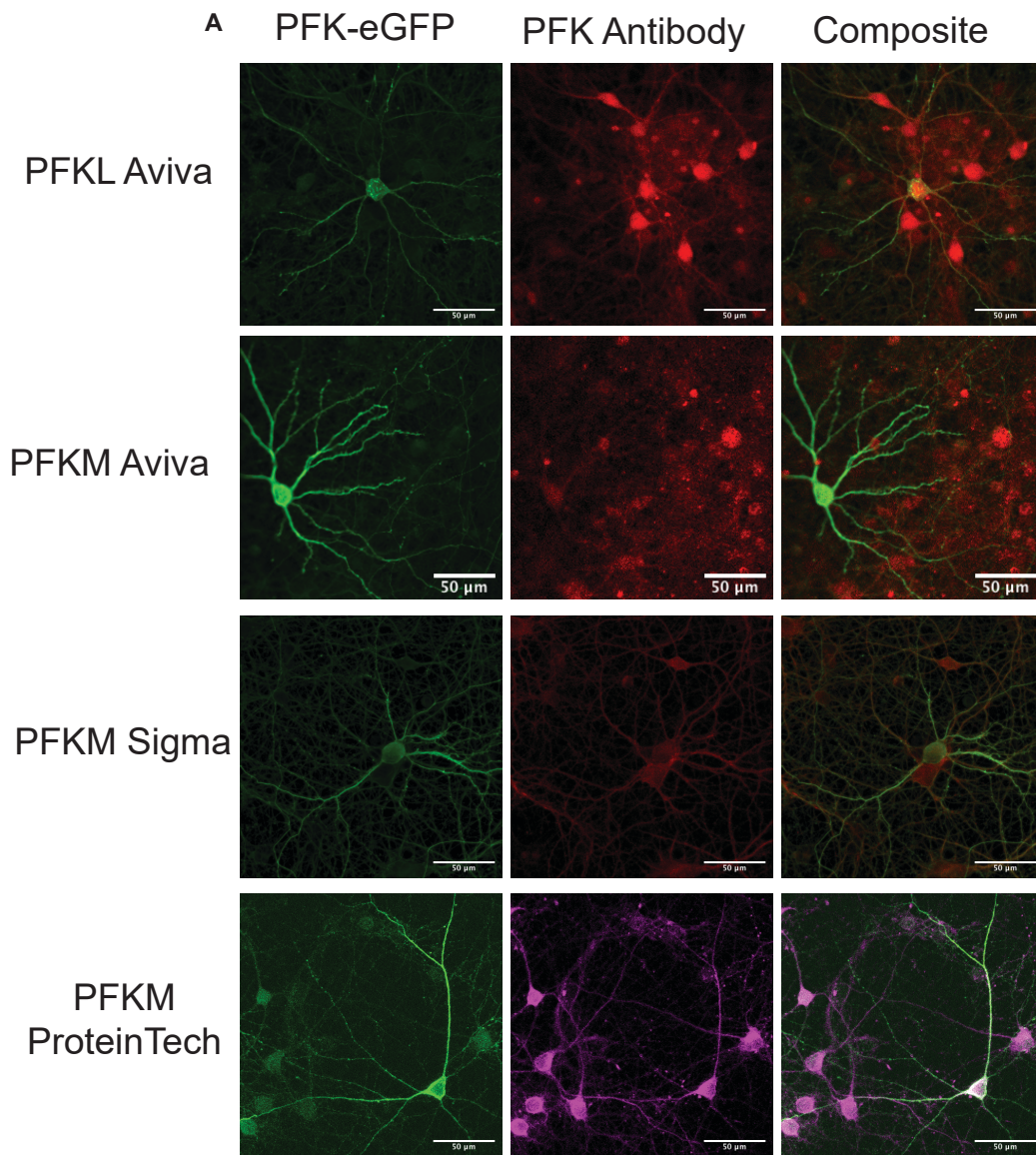
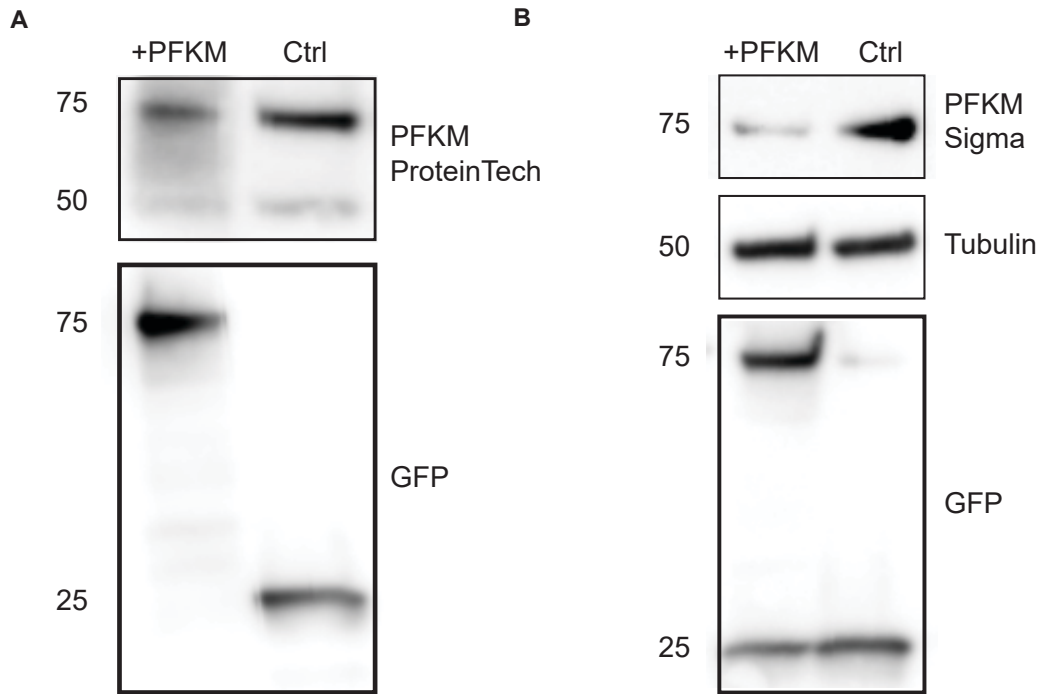


Figure 1.6. PFK displays presynaptic localization independent of TTX or KCl treatment. Neurons were transfected with vGlut1mCherry and either PFKLeGFP or PFKMeGFP and then treated with either TTX or KCl. The cells were then fixed and stained for mitochondria marker Tomm20. Representative images for neurons transfected with PFKLeGFP (A) or PFKMeGFP (B) and then treated with KCl are shown. Segments of axon were traced and the composite profile from all three channels are shown (C, D). Peak analysis was performed revealing a large percentage of vGlut1 peaks overlapping with a PFK peak (E). Data was analyzed between TTX and KCl treatment groups through t-test. No significant differences were found between TTX and KCl treatment groups. Scale bars represent 1um.

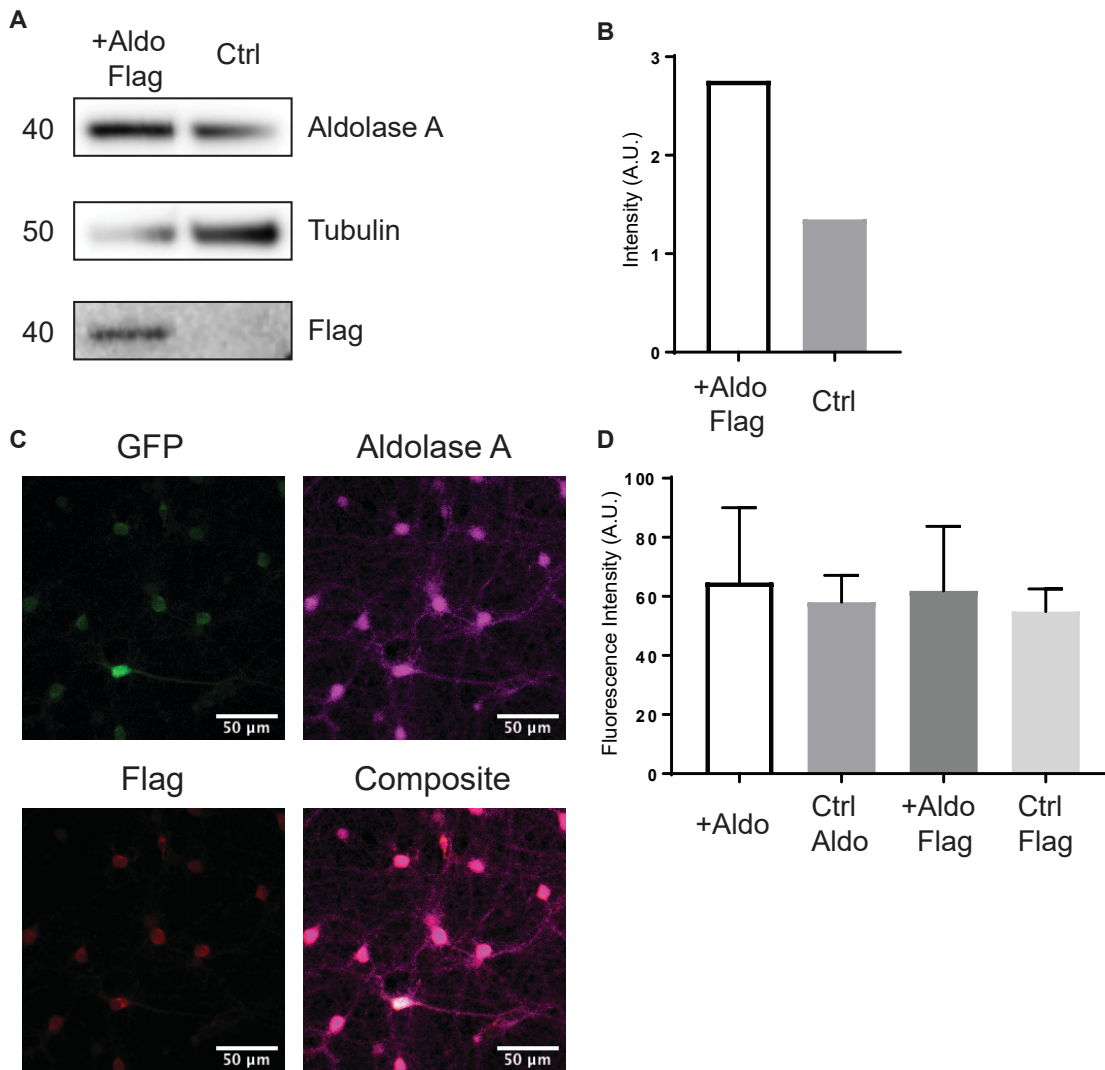


Supplementary Figure 1.1. PFK Antibody Validation for Immunocytochemistry. Various antibodies for PFK were tested using the corresponding overexpression constructs (A). Relative fluorescence between the somas of transfected neurons expected to express higher levels of PFK and neighboring cells were quantified (B). No antibody was able to detect significantly higher levels of fluorescence in transfected cells.



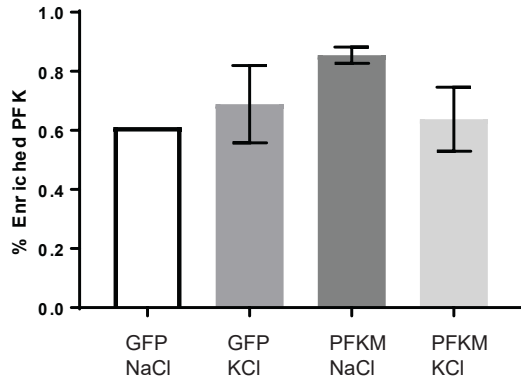
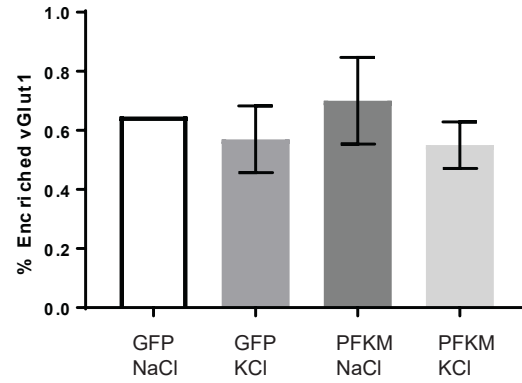
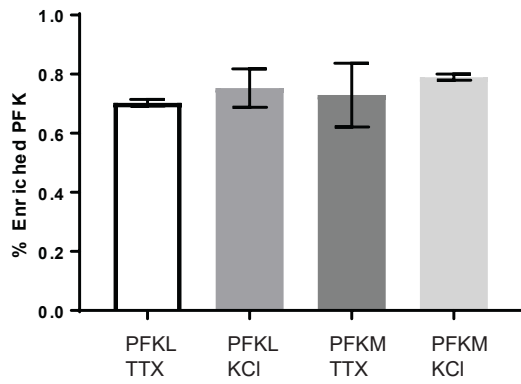
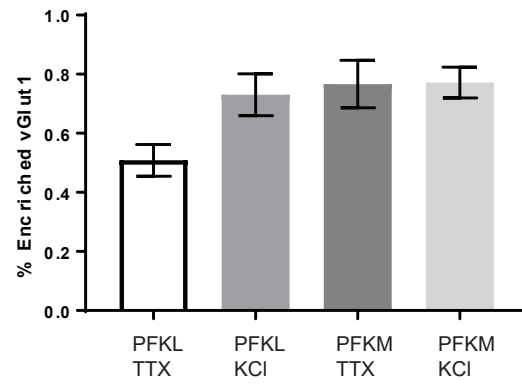
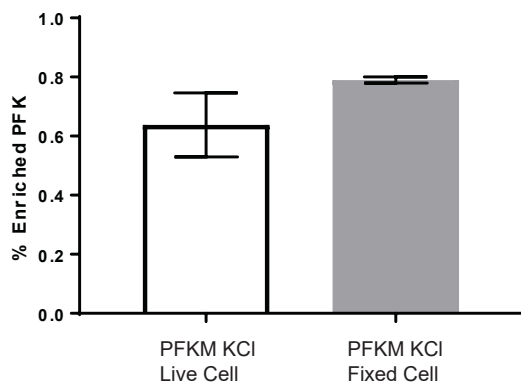
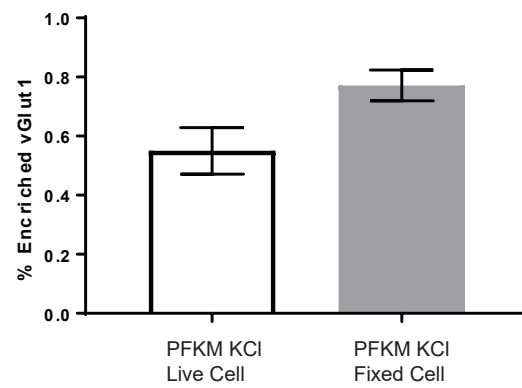


Supplementary Figure 1.2. PFKM Antibody Validation for Western Blot. HEK293T cells were transfected with either PFKMeGFP or GFP (control) and lysed for western blot. Antibodies PFKM ProteinTech (A) and PFKM Sigma (B) were tested. A matching GFP blot was tested revealing a band at 75kD in neurons transfected with PFKMeGFP. Both PFKM antibodies found this band in both PFKM and control conditions. The presence of this band at 75 kD in both the GFP blot and the control provide inconclusive results to the working of each PFKM antibody.



Supplementary Figure 1.3. Aldolase A Construct and Antibody Validation. HEK293T cells were transfected with flag-tagged aldolase or GFP (control) and lysed for western blot (A). Both a flag band corresponding to Aldolase A and higher levels of Aldolase (B) were found in the aldolase transfected HEK cells, indicating a working antibody and construct. Cortical neurons were transfected with the Aldo-Flag construct and immunostained for aldolase and flag (C). Both aldolase and flag fluorescent signals appeared only marginally higher in transfected cells, indicating either the construct or antibody may not be working properly for immunocytochemistry (D).

Supplementary Figure 1.4. Comparison of KCl Treatment between Live and Fixed Cell Imaging. Neurons were transfected with vGlut1mCherry and one of GFP, PFKLeGFP, or PFKMeGFP. Neurons were then treated with TTX overnight and changed to media containing either NaCl or KCl and live cell imaged immediately after. Peak analysis was performed comparing the fraction of vGlut1 peaks with a corresponding PFK peak (% enriched vGlut1) (A) or the fraction of PFK peaks with a vGlut1 peak (% enriched PFK) (B). No significant differences were found between treatment groups by t-test. Similarly, transfected neurons were treated overnight with TTX and then either left in TTX or changed to media containing KCl. An hour after treatment, neurons were fixed and immunostained. Peak analysis was performed again on vGlut1 enrichment (C) and PFK enrichment (D). To ensure that there were not localization differences between live and fixed cell imaging we compared the vGlut1 enrichment (E) and PFK enrichment (F) in neurons transfected with PFKM and treated with KCl. We found no significant differences, but there was a clear trend towards increased enrichment in fixed cell conditions. Neurons come from two separate independent preparations for live and fixed cell conditions.

A**Live Cell Peaks Analysis Enriched PFK****B****Live Cell Peaks Analysis Enriched v Glut1****C****ICC Peaks Analysis Enriched PFK****D****ICC Peaks Analysis Enriched v Glut1****E****Live Cell v. ICC Enriched PFK****F****Live Cell v. ICC Enriched v Glut1**

Materials and Methods

Cell culture

HEK293T cells were obtained from the American Type Culture Collection (Manassas, VA) and grown in T-75 flasks in Dulbecco's Modification of Eagle's medium (DMEM) supplemented with 10% heat inactivated fetal bovine serum (FBS) (Sigma-Aldrich, St. Louis, MO), 1% penicillin-streptomycin and 2mM glutamine (PSG) (Thermo Fisher Scientific, San Diego, CA). Cells were grown in T-75 (25cm²) flasks in a humidified 5% CO₂ incubator at 37°C. Cortical neurons were dissected and dissociated from E16-18 rat embryos (Hsd:Sprague Dawley® SD®) and resuspended in Neurobasal media (Life Technologies) with PSG, then plated on Poly-L-Lysine (PLL) (Sigma Aldrich) and Laminin (Life Technologies)-coated plate. The media was changed to Growth Media consisting of Neurobasal media supplemented with B27 supplement (Life Technologies) and PSG after two hours of incubation.

Antibodies and Constructs

The following antibodies were used: Rabbit anti-PFKM (ProteinTech, 55028-1-AP), Rabbit Anti-PFKM (Aviva, ARP61168), Rabbit Anti-PFKL (Aviva, ARP45774), Rabbit Anti-PFKM (Sigma Aldrich, HPA002117), Mouse Anti-Aldolase A (SantaCruz Biotechnology, sc-390733), Anti-Rabbit Tomm20 (Sigma Aldrich, HPA011562), Rabbit-Anti-Flag (ThermoFisher Scientific, PA1-984B), Chicken anti-GFP (Novus Biologicals, NB100-1614), Rabbit anti-GFP (Invitrogen, A11122), Mouse Anti-Actin (Sigma Aldrich, A2228), Mouse Anti-Tubulin (BioLegend, MMS-435P), Goat Anti-Chicken Alexa 488

(Life Technologies, A11039), Goat Anti-Rabbit Alexa 568 (Life Technologies, A11036), Goat Anti-Rabbit Alexa 647 (Invitrogen, A21245), Goat Anti-Mouse Alexa 568 (Life Technologies, A11035), Donkey Anti-Mouse Alexa 647 (Jackson ImmunoResearch, 715-605-151), Goat Anti-Rabbit Peroxidase AffiniPure (Jackson ImmunoResearch, 111-035-144), Goat Anti-Mouse Peroxidase AffiniPure (Jackson ImmunoResearch, 111-035-166).

The following constructs were used: PFKL-eGFP [21], PFKM-eGFP [21], MitoDsRed, eGFP, vGlut1-mCherry, Aldolase-Flag (Genscript, OMu13375D), CAMPARI [20], OGT.

Neuron Transfections

Neurons were transfected with Lipofectamine 2000 (Invitrogen) mixed with 0.5 ug DNA per plasmid per well in Pure Neurobasal (Life Technologies). Neurons were incubated for 25-45 minutes after the addition of DNA. Neurons were imaged or fixed 3 days after transfection.

HEK293T Transfections

HEK293T cells were transfected with CaCl₂ and HBS (Life Technologies) mixed with 1.5 ug DNA per plasmid per well. CaCl₂, ddH₂O, and DNA were all added to tube. Then HBS was added slowly and then bubbled. The solution was rested for 10 minutes, then 320 uL per well was added. Western Blots were either performed the following day or the two days after transfection depending on plated cell density of HEK cells.

Immunocytochemistry

Immunocytochemistry was performed on DIV13-15 cortical neurons. Cells were fixed with 4% PFA (Fisher Scientific) / 4% Sucrose (Sigma Aldrich) in PBS for 15 minutes, then washed 3 times with PBS in 5 minute intervals. Neurons were blocked for 30 minutes with blocking solution containing 1% BSA (Genesee Scientific), and 0.5% Saponin (Sigma) in PBS. They were then treated with primary antibody diluted in blocking solution and left to shake overnight at 4° C. The following day they were washed three times with PBS at 15 minute intervals. Cells were then treated with secondary antibody diluted in blocking solution for 1 hour at room temperature, Washed three times again at 15 minute intervals, and finally mounted on glass slides with Fluoromount-G (SouthernBiotech).

Live Cell Imaging

Transfected neurons were washed with Hibernate E (Life Technologies) containing wither 0uM or 1uM TMG depending on condition. Coverslips were then transferred to the imaging chamber where the corresponding Hibernate E was added. Time lapse images were taken at 40x magnification and an image was taken every 5 seconds for 50 frames. Neurons were imaged for at most 30 minutes and then discarded.

Drug Treatment

For TMG treatment, cortical neurons were treated with 2uM TMG (EMD Millipore) overnight the day before live-cell imaging. For TTX and KCl treatment, Cortical neurons

were treated with 1 μ M TTX (Tocris) and 50 μ M AP5 (Tocris) overnight before fixation. The following day, neurons treated with KCl would be changed to depolarization media containing 55mM KCl for 1 hour and then fixed. Depolarization media consisted of 170mM KCl, 10mM HEPES 7.4, 1mM MgCl₂, 2mM CaCl₂ diluted in growth media.

Western Blot

Cells were washed with PBS on ice, then lysed with cell lysis buffer consisting of 1% Nonidet P-40 (EMD Millipore), 15mM Tris-HCl pH 7.5 (MP Biomedicals), 150mM NaCl, 1mM EDTA pH 8.0 (Life Technologies), 1mM DTT (G-Biosciences), 0.1mM PMSF (UCSD CORE), and 1x Protease Inhibitor Cocktail (UCSD CORE) in ddH₂O. Cells were then spun down at 14xg for 15 minutes at 4° C. The supernatant was collected and mixed with 4x Laemli. The mixture was then boiled at 100° C for 5 minutes and then spun down at 14 rpm for 5 minutes. The mixture was run on a 4-20% gel (BioRad) at 100V until the bands had traveled all the way down the gel. The gel was then transferred to a nitrocellulose membrane for 90 minutes at 100A. The blot was then incubated with primary antibody overnight at 4° C. The following day, the blot was washed with PBST 3 times at 15 minute intervals, then treated with secondary antibody for 1 hour at room temperature, and finally washed with PBST 3 more times at 15 minute intervals before imaging. The blots were imaged using SuperSignal™ West Dura Extended Duration Substrate (Thermo Fischer Scientific) and the Azure c600 imaging system.

G6PD Activity Assay

HEK293T cells were either mock transfected or transfected with OGT and then treated with TMG. The activity assay was performed per manufacturer's protocol (abcam, ab102529). Data was normalized using BCA assay (Thermo Fischer Scientific) and western blot.

II. Developing SHCellAnalyzer: a semi-automated platform for *in-situ* assessment of cellular bioenergetics

Abstract

Every cell must constantly monitor its energy level and appropriately adjust energy production rates based on metabolic demand to maintain homeostasis. Energy homeostasis critically depends on tight coupling between cellular metabolism and mitochondrial function. Monitoring cellular metabolic pathways and mitochondrial activity in real time enable us to investigate homeostatic pathways. The Agilent Seahorse XF Analyzer is an ideal multi-well, plate-based platform to measure cellular metabolic activity and mitochondrial bioenergetics. While this platform expands the capacity to investigate metabolism in a myriad of different cell and tissue types, accurate data interpretation between different experimental conditions requires normalization. Prior methods for data normalization have included protein level measurement, cell fluorescence quantification, and cell counts per well. Of these methods, protein quantification may be inaccurate when a small amount of sample is assayed in 96-well format, fluorescence quantification may be prone to oversaturation and is often imprecise. *In situ* cell counts remain the most accurate and consistent means by which to normalize metabolic flux data. Fixation of cells and imaging upon assay completion can provide images with which to produce cell counts, but these depend on microscopes equipped to image multiple wells at a time such as Perkin Elmer's Operetta CLS. Fixation of cells at higher densities may also provide inaccurate cell counts with which to normalize data as cells may be disrupted upon additional fixation and washing steps. Here, we have developed a semi-automated platform, adaptable to any microscope for cell number quantification and established a protocol with which to stain cells. SHCellAnalyzer is composed entirely of free software that allows us to obtain cell counts with high correlation to plating density. The portability

and ease of access of SHCellAnalyzer has the potential to allow for a consistent normalization methodology in metabolic flux assays throughout samples.

Introduction

Metabolic reprogramming and dysregulation has been implicated in a multitude of disorders including cancer, diabetes, and neurodegeneration. Analyzing mitochondrial function provides essential information on metabolism in various tissues and cells. Mitochondrial function has been characterized by immunohistochemistry protocols through cytochrome-c oxidase (COX) or succinate dehydrogenase (SDH) staining in which a mosaic expression of COX or SDH enzyme activity in tissue may indicate mutations in mitochondria in various cells. Alternatively, respirometry measures O₂ consumption rate, and the addition of various substrates provides a ratio by which to assess mitochondrial coupling of O₂ to provide ATP for the cell.

With the advent of the XF metabolic flux analyzer, invaluable information about the major energy producing pathways of most cells: glycolysis and oxidative phosphorylation, can be quantitatively assessed to analyze mitochondrial function. The seahorse assay captures the metabolic profiles for oxidative phosphorylation and glycolysis by measuring oxygen consumption rate (OCR) and extracellular acidification rate (ECAR), respectively. OCR and ECAR are determined through several drug injections and readings measuring basal and maximal respiration, spare respiratory capacity, ATP production, proton leak, and nonmitochondrial respiration. The Seahorse XF Cell Mito Stress Test consists of a protocol that delivers oligomycin, carbonyl cyanide-4-phenylhydrazone (FCCP), and rotenone/antimycin to target components of the electron transport chain in the mitochondria. Oligomycin targets complex V by inhibiting ATP synthase, and the resulting decrease in OCR reveals the mitochondrial respiration associated with cellular ATP production. FCCP serves as an uncoupler that

collapses the proton gradient and determines the maximal respiration as electron flow is uninhibited and the mitochondria may work at full capacity. Rotenone and antimycin A are a complex I inhibitor and complex III inhibitor, respectively, that completely prevents mitochondria from respiring. As a result, a measurement of non-mitochondrial respiration is given.

In spite of the ability of this technology to acquire data crucial for understanding metabolic flux within a subset of mitochondria, normalization remains a constant challenge. Common methods for normalization include quantification of total protein, nuclear DNA, cell fluorescence, and cell count. While each method provides benefits, each has their own limitations. Quantifying total cellular protein is simple and inexpensive, but introduces potential error with small well sizes, and cannot be accurately performed in 96-well microplates. Cellular protein levels may also shift in response to drug treatment in cases where mitochondrial biogenesis is assessed. Nuclear DNA quantification is another potent normalization method that removes some of the drawbacks of measuring total cellular protein, but still introduces its own restrictions. Measuring nuclear DNA can only be used for mono-nucleic cells, and cannot be used for multi-nucleic cells such as cardiomyocytes. DNA levels do not fluctuate, however, and thus can be used independently of the type of research. Total cellular fluorescence is useful, but requires proper image acquisition and thresholding for accurate quantification of fluorescent intensity. Fluorescence is also prone to variability between samples and may provide inaccurate or inconsistent data. Gathering cell counts for normalization is time consuming and expensive when acquiring images for a multi-well microplate. Assessing cell counts manually is also inefficient.

Despite the limitations of the methods mentioned, cell counting provides the least experimental restrictions. Providing reliable cell counts typically requires an automated instrument to produce counts in a reasonable timeframe. There remains to be an efficient and cost-effective tool for normalization by cell counts for microplates with multiple wells. Currently, instruments that can perform automated cell counting on multi-well microplates include Agilent's BioTek Cytation 5 and Perkin Elmer's Operetta CLS. These automated instruments are often time-consuming, however, as they take hours to obtain images, and may not be the most cost-effective. To address these issues and to provide a standard method with which to normalize metabolic flux data, we present a platform independent approach to normalize through cell count composed entirely of freeware. SHCellAnalyzer provides a clean, streamlined approach for counting cells within a given region of interest in microplate wells, and extrapolates that value to whole wells for proper normalization of metabolic flux data. This tool is invaluable as it is accessible, efficient, inexpensive, and provides an accurate and consistent means by which to meaningfully interpret metabolic flux data. Here we outline an optimized approach by which to obtain accurate cell counts through proper image acquisition and calibration of SHCellAnalyzer for various cells types. Cell counts gathered from SHCellAnalyzer have been accurate and true to stated plating density, and provides a cost-effective, systematic, and powerful tool for normalization.

Results

SHCellAnalyzer: A tool for normalizing metabolic flux data

We developed SHCellAnalyzer, a fast and semi-automated program, to simplify the process of normalizing metabolic flux data. The program uses images of the wells taken immediately after the metabolic flux assay (Fig 2.1). These images must be sufficiently high resolution for SHCellAnalyzer to distinguish individual cells from each other and obtain an accurate cell count. Accordingly, images obtained often cannot both contain the whole well and provide the resolution necessary to distinguish individual cells. By sampling the wells with just a few images and averaging them, a relatively accurate count can be obtained with a tradeoff in variability. Accordingly, SHCellAnalyzer consists of two separate programs: The ImageJ macro, SHCellCounter, which counts the cells in the obtained images, and a Python script, SHCellProcessor, which converts the raw counts from SHCellCounter into representative counts for the imaged well (Fig 2.2). SHCellCounter first makes the images binary by thresholding them, either with an automated algorithm or manually. SHCellCounter then performs a watershed operation to define the lines between adjacent cells. Then, cells larger than a specified size are counted in regions of interest (ROIs) defined by the user. SHCellProcessor takes these counts as input and extrapolates them to represent the entire well. To do so, SHCellProcessor uses the size of the regions where the cells were counted alongside the seeding area of the well to create an estimated cell count for the well. As a tool, SHCellAnalyzer is semi-automated and requires configuration from the

user before each run and calibration of the macro for any particular set of imaging conditions.

Configuration and Calibration of SHCellCounter

SHCellCounter has four parameters that require configuration before each run: Thresholding Algorithm, Cell Size Cutoff, ROI Determination, and Alignment. The thresholding algorithm affects which pixels in the image are recognized as cells. The cell size cutoff defines the size of the smallest particle that will be considered a cell. Proper configuration of these two parameters is critical to obtain accurate cell counts. ROI Determination can be used to generate ROIs that avoid unrepresentative data within an image, such as the standoffs in 96 well plates. The Alignment option can be used alongside ROIs to ensure the same areas within each image are excluded.

To count cells, SHCellCounter must first distinguish which pixels represent cells. We employ two automated thresholding algorithms, Otsu and Huang, to appropriately threshold images depending on the signal to noise ratio of the cells against the background (Fig 2.3A). By default, SHCellCounter uses Otsu, which thresholds the image by maximizing the separation between the foreground and background [17]. Accordingly, Otsu is an appropriate algorithm for images with distinct cells and low background signal (Fig 2.3B). However, for analyzing images with more faint cells, Otsu often has difficulty detecting the fainter signals, as their gray values more closely resemble background than foreground (Fig 2.3C). By contrast, We incorporated the Huang thresholding algorithm into SHCellCounter to analyze images where the cells did not express NucBlue as strongly (Fig 2.3C). Huang more appropriately thresholds these

images by attempting to minimize the fuzziness of the image, which can more accurately separate the cells from the background when the valley between the two is not as distinct [18]. Huang is not the default thresholding algorithm of choice because it will often threshold adjacent cells together, resulting in larger blobs and underestimated cell counts (Fig 2.3B). Thus, Images with visually distinct cells should be thresholded with Otsu, whereas noisy images with faint cells blending into the background should be thresholded by Huang (Fig 2.3A). In the case where neither algorithm provides an adequate threshold, the user can also manually set the threshold for their images. This is generally not recommended as the user sacrifices the consistency of an automated thresholding algorithm but left as a fail-safe if truly neither algorithm is appropriate.

Images are not perfect and contain small noisy particles that should not be counted as cells. SHCellCounter ignores these particles by defining a cell size cutoff below which particles are defined as not cells. SHCellCounter has two modes to establish a cutoff, Entry and Calibration (Fig 2.4A). Entry mode allows the user to input an established cutoff and obtain accurate cell counts. However, for the user to obtain an appropriate cutoff, it must be calibrated to the cell type and imaging conditions. Calibration mode enables the user to easily determine an optimal cutoff by testing multiple at a single time (Fig 2.4B). First, the user inputs a range of cell size cutoffs to test and SHCellCounter will count the image at all those cutoffs. Then, the user will have to manually count their test set of images. Finally, the user can run SHCellCalibrator, a short python script which will compare your automated counts to your manual counts and determine which cell size cutoff yielded the best results with no significant difference from the manual counts. In doing so, an optimal cell size cutoff will

be obtained which will produce accurate cell counts. If none of the automated counts can sufficiently recapitulate the manual counts, SHCellCounter will be unable to accurately count the given cells with the given imaging conditions. In this case, the cells of interest may need to be imaged at a higher magnification to produce a higher resolution to be accurately counted by SHCellCounter.

The ROI Generation feature of SHCellCounter allows the user to exclude specific regions of an image which may contain outlier data. The standoffs present in 96 well plates, for example, represent a constant area which must be excluded from cell counting. SHCellCounter provides the user with four options to generate ROIs: None, Current, Directory, and Manually (Fig 5A). Many images will be able to avoid the standoffs, especially when imaging at higher magnifications. In these cases, the None option will use no ROIs and simply counts the entire image. If ROIs are needed, they can be generated in a variety of ways (Fig 2.5B). By selecting Current, SHCellCounter will use all the ROIs currently in the ROI Manager. This is very convenient for consecutively running distinct sets of images that require the same set of ROIs or testing ROIs to ensure they exclude the appropriate areas of the image. The Directory option opens an a set of saved ROIs, enabling the user to consistently use the same ROIs for all their cell counting data. Finally, if no prior ROIs exist the user can select the Manually option to create ROIs while running SHCellCounter. By incorporating the use of ROIs, SHCellCounter is able to specifically exclude the standoffs that are continually present in Agilent's 96 well plates.

While ROIs are a powerful tool for excluding regions of disinterest, those regions may differ between images. Specifically, in 96 well plate images including multiple

standoffs, the images may be offset such that an appropriate ROI for one image results in the incorporation of a standoff for another (Fig 2.6A). One potential solution is to attempt to align images with common features, such as the standoffs, so that the ROIs used exclude the proper areas in each image. SHCellCounter uses StackReg for its image alignment algorithm which allows it to quickly and automatically align a stack of images obtained from multiple wells of the 96 well plate [19]. Most image alignment algorithms are designed to align exactly identical, but offset features in an images. However, with only similar features such as standoffs, alignment can still help set the images to the same place (Fig 2.6B). Alongside the usage of ROIs, the alignment feature allows for the exclusion of standoffs in images of 96 well plates.

Calibration of SHCellCounter Ensures Accurate Counting

C2C12 (cells and HEK293T (human embryonic kidney) cells were trypsinized and seeded overnight on 96-well microplates prior to the metabolic flux assay. When using cell counts with which to normalize metabolic flux data, proper imaging conditions with appropriate magnification for each cell type is necessary. Cells may differ in size and their tendency to cluster together ensures appropriate configuration to count cells accurately for normalization of metabolic flux data. Calibration of cell size cutoff on SHCellCounter and use of SHCellCalibrator allows the user to determine the best cell size cutoff parameter and the best magnification settings for each cell type. Here we plated C2C12 and HEK293T cells and imaged individual wells upon completion of the metabolic flux assay. C2C12 cells were imaged at 4x and 10x magnification, and HEK293T cells were imaged at 40x. Magnification settings were initially chosen to

ensure that cells could distinctly be resolved from background and adjacent cells prior to further calibration and determination of best magnification settings. For both cell lines at differing magnification settings, a minimum cell size cutoff ranging from 0-25 μm^2 with step sizes of 5 μm^2 was used to determine the appropriate magnification and cell size cutoff for each cell type. Manual counts were obtained to compare to automated cell counts at differing cell size cutoffs. Cell counts obtained manually and with SHCellCounter at varying cell size cutoffs were plotted against each other (Fig 2.7A-C). We then used SHCellCalibrator to determine which cell size cutoff was optimal by comparing each set of counts with the manual counts. We then plotted the counts from the optimal cell size cutoff against the manual counts (Fig 2.7D-F). A perfectly linear relationship depicts that the counts gathered were as close to the estimated plated cell density as possible. C2C12 cells imaged at 4x magnification using cell size cutoff 5 μm^2 showed the closest relationship to the estimated plating cell density and the manual counts (Fig 2.7D). However, there remains a significant difference between counts obtained manually and counts generated automatically. Therefore, imaging C2C12 cells at 4x magnification is not sufficient to produce accurate cell counts. The best cell size cutoff for C2C12 cells imaged at 10x magnification was found to be 15 μm^2 (Fig 2.7E). The corresponding linear relationship between the automated and manually-obtained cell counts shows that this cell size cutoff and magnification is sufficient to produce accurate counts. To calibrate cell size cutoff and magnification for a different cell type, HEK293T cells were imaged at 40x magnification. The best cell size cutoff used to produce accurate cell counts was 10 μm^2 (Fig 2.7F). Therefore, this calibration allows the user to best determine the magnification power necessary to delineate individual

cells from background and from neighboring cells. It also helps the user determine the minimum cell size cutoff by which SHCellCounter can distinguish cells appropriately without overcounting smaller pixels or undercounting cells in clusters.

SHCellAnalyzer Normalizes Variance in HEK293T Cells and Neurons

Normalization of metabolic flux data to cell counts is necessary to gather meaningful data. Therefore, we plated HEK293T cells at varying plating densities to reveal the shift of trends in metabolism between unnormalized and normalized data. Unnormalized HEK293T cells plated at higher densities show a shift towards having increased levels of oxygen consumption rate (OCR) throughout the assay (Fig 2.8A, C). However, upon normalization with accurate cell counts obtained from SHCellAnalyzer, OCR values were brought to a similar baseline level across varying plating densities (Fig 2.8B, D). This is expected since fundamentally, HEK293T cells will have the same overall metabolic flux, but may differ slightly when seeded at higher or lower densities. This also depicts the importance of normalization via cell counts as misleading data may be generated if prior to normalization, cells plated at higher densities simply seem more metabolically active due to their high plating density (Fig 2.8C). We similarly normalized metabolic flux data from Neurons plated at 100K cells per well. From the unnormalized data, one of the independent experiments performed appeared to be an outlier with much lower overall OCR values (Fig 2.8A). However, upon normalization all experimental replicates were brought to similar values after each drug injection (Fig 2.8B, C). We show that shifted OCR values from both intentional and unintentional

plating variance could be corrected via normalization through cell counts obtained by SHCellAnalyzer.

Discussion

Metabolic flux assays are a powerful tool for understanding the everchanging regulation of ATP production in the cell. However, because these are plate based cellular assays, the amount of cell on the plate can greatly impact the output. Normalization of metabolic flux data is therefore key to obtaining meaningful data on the rates of glycolysis and oxidative phosphorylation. We describe here a simple, effective program for normalizing metabolic flux data in SHCellAnalyzer. SHCellAnalyzer can provide consistent and accurate cell counts from normalization, a task that previously required a dedicated cell counting instrument. Labs that have access to a powerful instrument such as Operetta or the BioTek Cytation clearly do not have a need for SHCellAnalyzer. However, labs who do not have access and cannot afford to purchase these expensive instruments now have another option to normalize their metabolic flux data through cell counts. While powerful and useful, SHCellAnalyzer is not the only cell counting software out there. CellProfiler is a relatively well known cell counting program that could be made to count cells much like SHCellAnalyzer. Labs with individuals very experienced with CellProfiler may prefer to use familiar software as opposed to learning a new program in SHCellAnalyzer. However, SHCellAnalyzer streamlines the process of acquiring images by having a built-in method to extrapolate images that only sample a well to estimate the cell count for the entire well. Though these estimates may lead to some increased variance in the cell counts, we show that these counts follow a linear pattern that matches plating density and therefore lead to a consistent metric for normalization. Ideally, the cell counts obtained with SHCellAnalyzer could be validated through an established cell counting instrument, such as Operetta to ensure the

accuracy of SHCellAnalyzer cell estimates relative to the entire well. Nevertheless, SHCellAnalyzer provides a powerful and accessible feature that enables any lab to normalize metabolic flux data through cell counts.

Figures

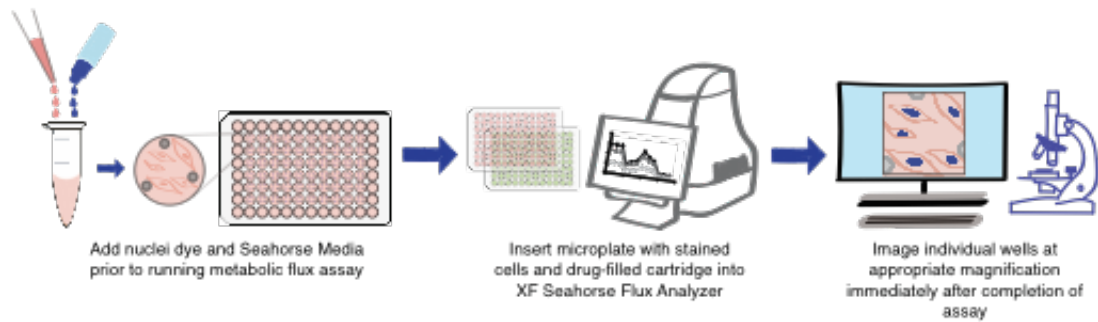
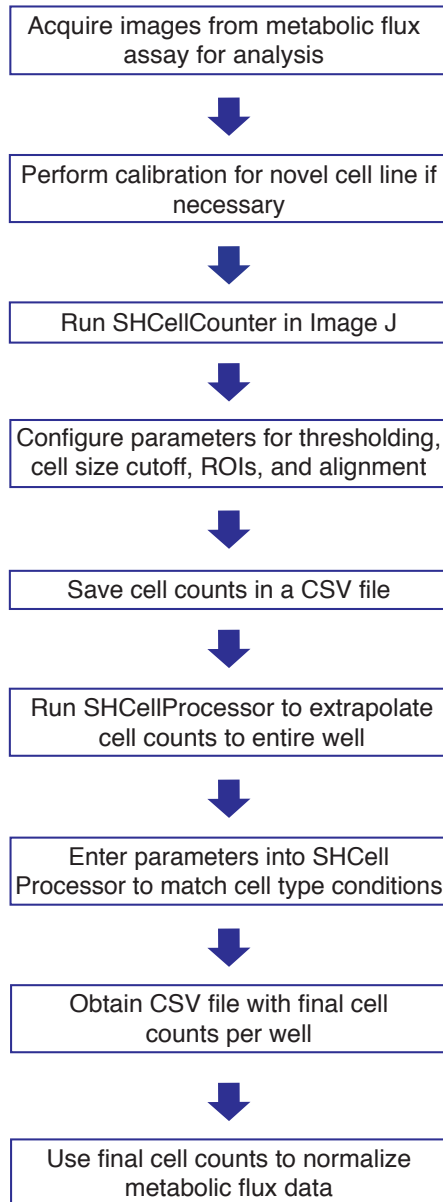


Figure 2.1. Metabolic Flux Assay Workflow. Seahorse media and nuclei dye (NucBlue) are premixed, and then added to wells during media exchange prior to metabolic flux assay. Plates are placed in XF Metabolic Flux Analyzer for OCR and ECAR measurements. Portions of individual wells are imaged via nuclei stain using DAPI filter at appropriate magnification. These images are then used to obtain cell counts for normalization.

Figure 2.2. SHCellAnalyzer Workflow. Images are acquired upon completion of metabolic flux assay. Calibration for novel cell type is performed and SHCellCounter is run with various cell size cutoffs. Given the appropriate cell size cutoff, ROIs, thresholding, and alignment, parameters are configured. Cells are counted in SHCellCounter and files are saved in a CSV file. SHCellProcessor uses preliminary counts to estimate the total cell count for the individual well from counts produced in SHCellCounter. Configure parameters to run SHCellProcessor, then obtain final counts per well in another CSV file. These final counts are then used for normalization via Agilent's seahorse software.



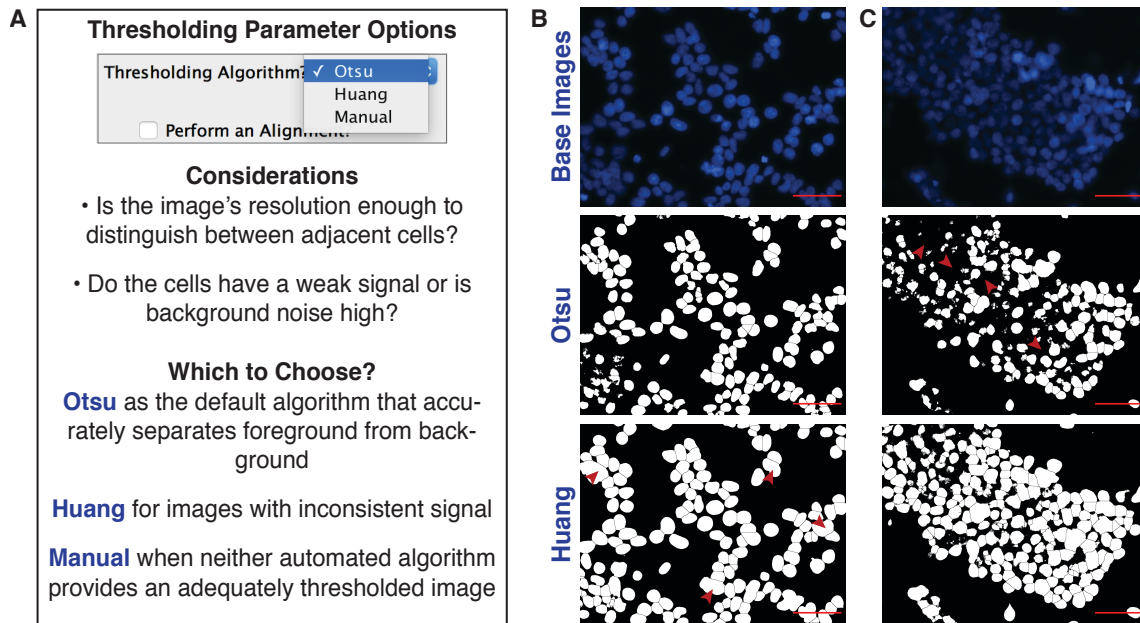


Figure 2.3. Thresholding Algorithm Parameter Determination. Options available for thresholding and considerations and reasoning for how to choose between Otsu, Huang, and Manually (A). Example images optimally thresholded using either Otsu (B) or Huang (C). Base image in panel B has good signal to noise ratio and the cells are effectively picked out from the background with Otsu. In this case, Huang includes too much of the background and causes some individual cells to be analyzed as clumps as shown in red arrows. Base image in panel C has low contrast between the background and cells. In this case, Otsu is unable to properly identify the cells in the background, while Huang can pick out these cells that appear more dim. If neither Otsu nor Huang can properly threshold the cells, the user can attempt to Manually configure the thresholding such that cells are effectively delineated from background and other cells as to avoid over- or under-counting. Scale bar = 50 μm .

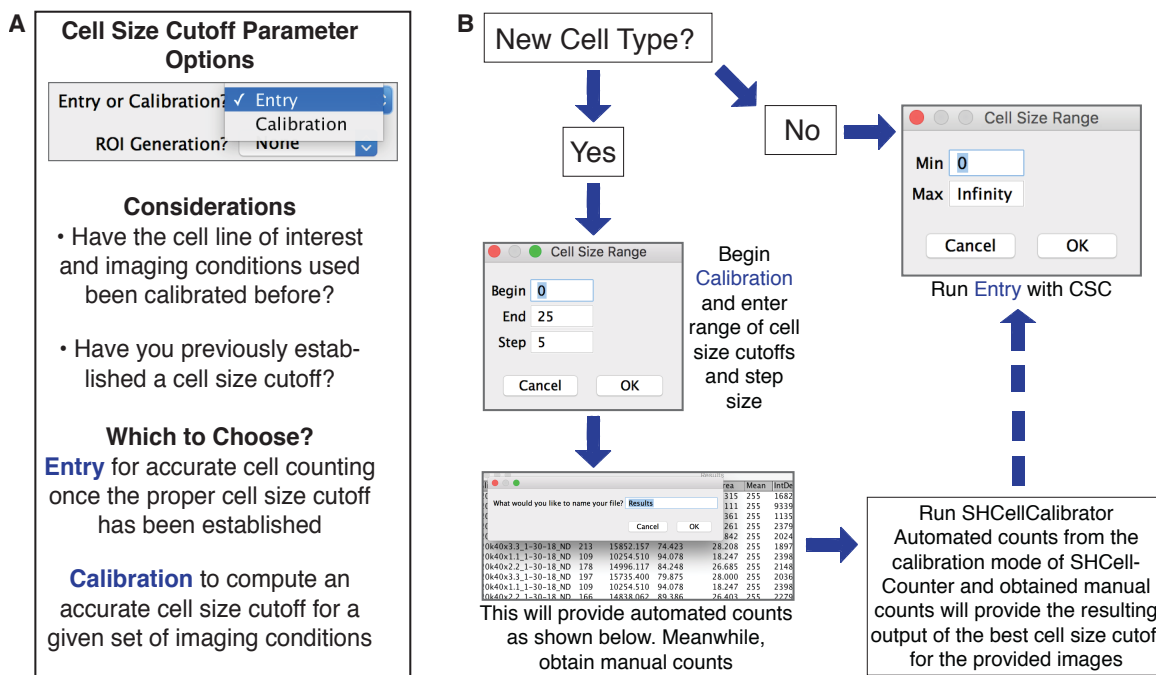


Figure 2.4. Cell Size Cutoff (CSC) Parameter Determination. Options available for CSC, and considerations and reasoning for how to choose between Entry, and Calibration (A). Workflow (B) for using either the Entry or Calibration option. Calibration mode counts the cells at a variety of CSCs. These automated counts can be compared to manual counts in SHCellCalibrator to determine the optimal CSC for new cell types. Once a CSC is obtained, it can be entered and used in Entry mode. Scale bar = 100 μm .

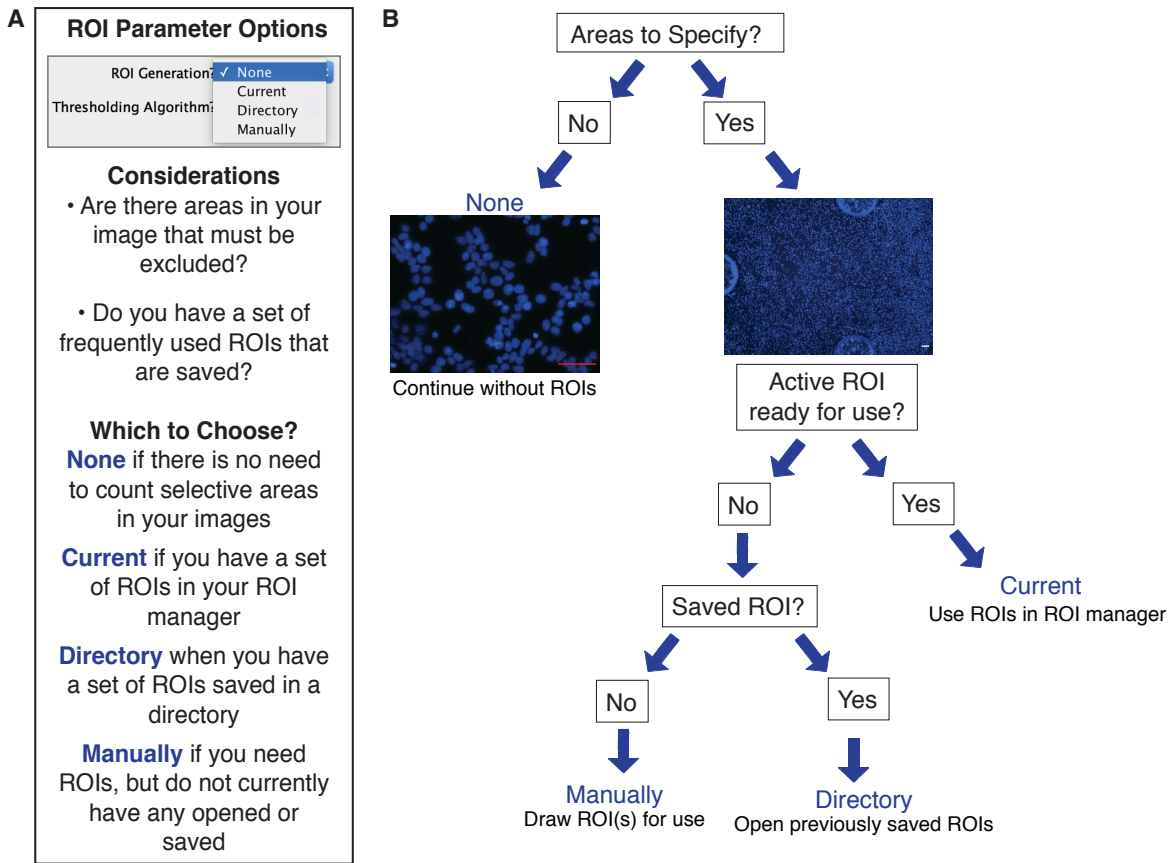


Figure 2.5. Region of Interest (ROI) Parameter Determination. Options available for ROI generation and considerations and reasoning for how to choose between None, Current, Directory and Manually (A). Combined workflow (B) for using each of the four options. Choosing None will simply continue running SHCellCounter without using any ROIs. Choosing Current will use any ROIs currently in the ROI manager in ImageJ. Choosing Directory will prompt the user to select a folder containing previously saved ROIs. SHCellCounter will then use those ROIs for cell counting. Choosing Manually will prompt the user to create their own ROIs which the macro will then use.

A Alignment Parameter Options

Perform an Alignment?

Considerations

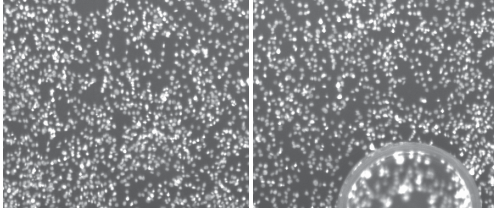
- Are there areas in your image that must be excluded?
- Are there common features across all your images?

Which to Choose?

No if the answer to either question is no

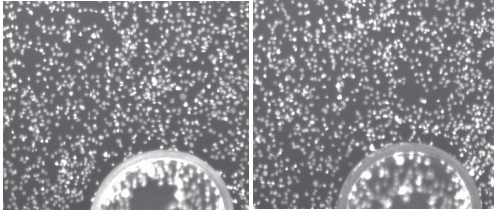
Yes if the answer to both questions is yes, and you want to align the images to common features to consistently exclude the same regions

B



Perform an Alignment?

C



Perform an Alignment?

Figure 2.6. Alignment Parameter Determination. Considerations and reasoning for whether or not to align images (A). Example images that either should not (B) or should (C) be aligned. Set of images in B lack a common defining feature (for Seahorse Metabolic Flux Assays usually a standoff in the wells), and therefore have no reason to be aligned. The second set of images (C) both contain a standoff which they may be aligned to. A single ROI can be used to exclude the standoff in all the aligned images.

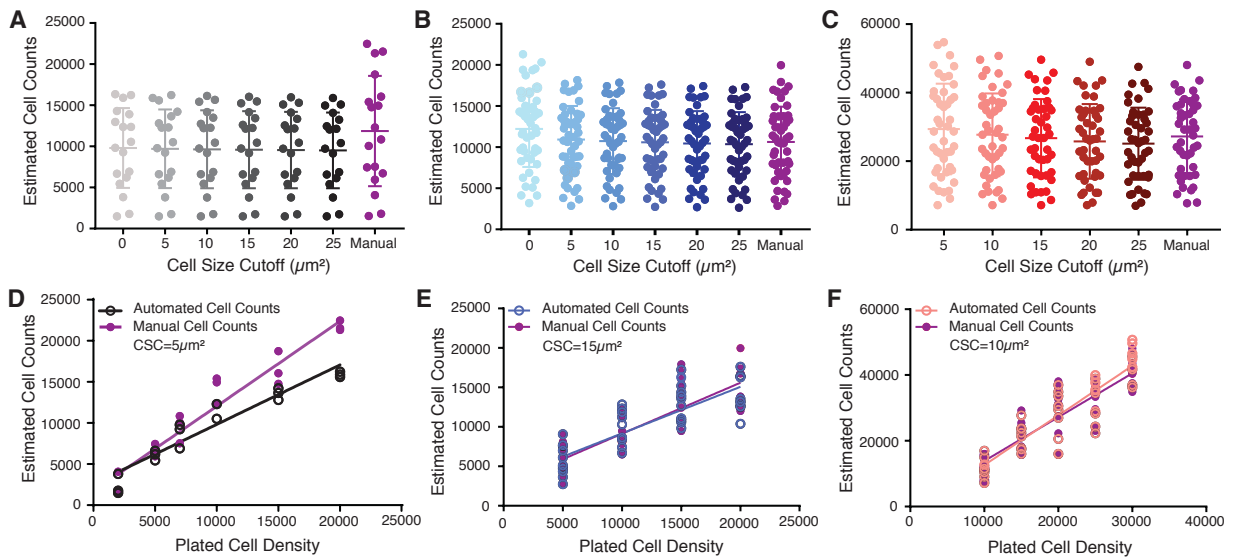
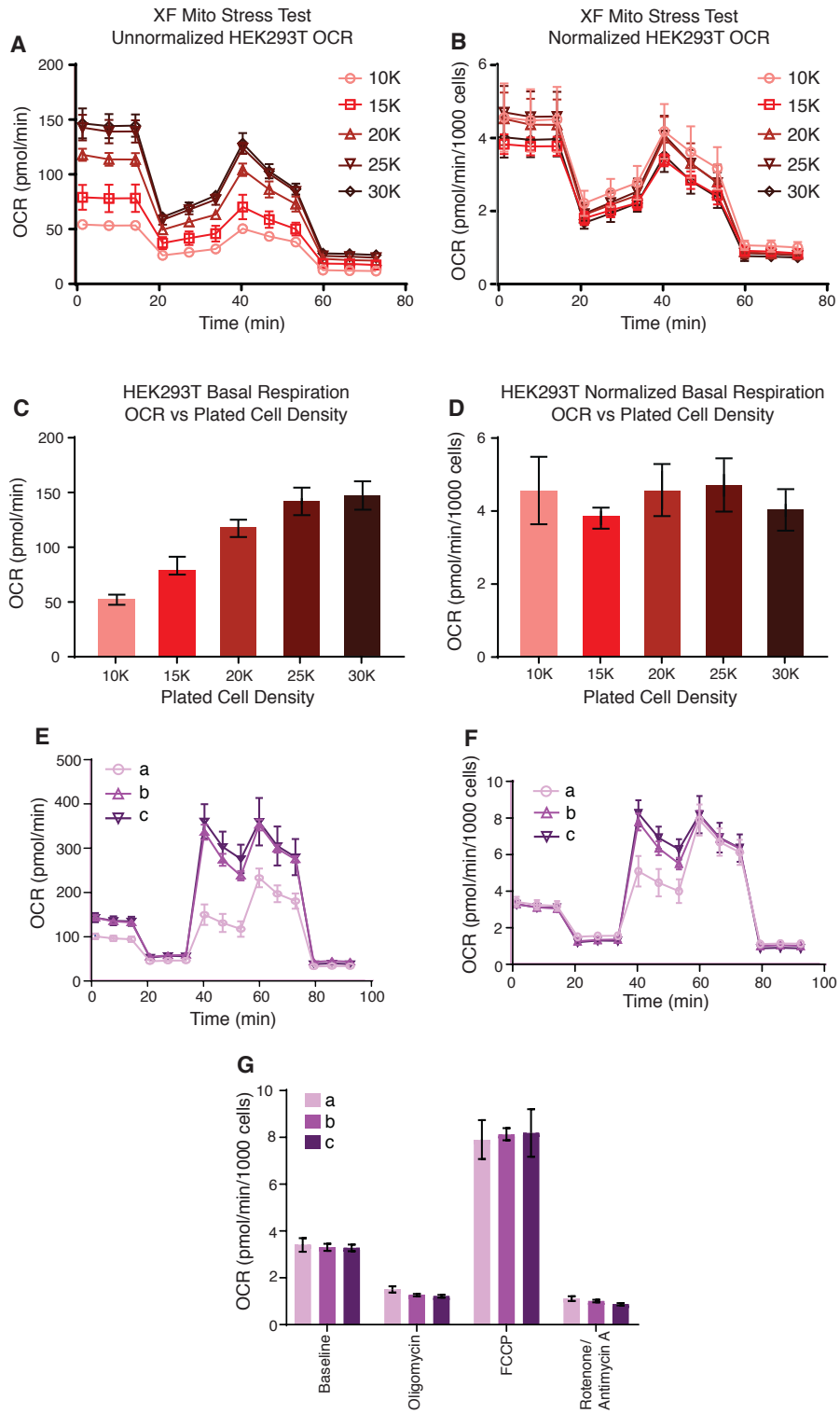


Figure 2.7. Cell Size Cutoff Validation. Automated counts obtained with SHCellAnalyzer compared to manual counts of the same images for C2C12 cells imaged at 4x magnification (A), C2C12 cells imaged at 10x magnification (B), and HEK293T cells imaged at 40x magnification (C). Comparison of manual counts with counts obtained at the best cell size cutoff for C2C12 cells imaged at 4x magnification (D), C2C12 cells imaged at 10x magnification (E), and HEK293T cells imaged at 40x magnification (F). Determination of cell size cutoffs using automated and manual cell counts show optimal CSC= $15\mu\text{m}^2$ for C2C12 at 10x magnification, and CSC= $10\mu\text{m}^2$ for HEK293T at 40x magnification.

Figure 2.8. Metabolic Flux Data for HEK293T cells and Neurons. Unnormalized (A) and normalized (B) OCR data was obtained for HEK293T cells plated at densities ranging from 10K to 30K. Baseline OCR values (time = 0 min) for HEK293T cells were plotted across densities without normalization (C) and with normalization (D). Normalization removed significant differences between groups with different plating densities. Unnormalized (E) and normalized (F) OCR data was obtained from cortical neurons from three independent preparations (a, b, and c). Normalization of OCR data reduced the variation between the three groups at baseline and after injections of Oligomycin, FCCP, and Rotenone with Antimycin A (G). Arrows on graphs depict timepoints for various drug injections throughout duration of metabolic flux assay.



Materials and Methods

Cell culture

C2C12 and HEK293T cells were obtained from the American Type Culture Collection (Manassas, VA) and grown in T-75 flasks in Dulbecco's Modification of Eagle's medium (DMEM) supplemented with 10% heat inactivated fetal bovine serum (FBS) (Sigma-Aldrich, St. Louis, MO), 1% penicillin-streptomycin and 2mM glutamine (PSG) (Thermo Fisher Scientific, San Diego, CA). Cells were grown in T-75 (25cm²) flasks in a humidified 5% CO₂ incubator at 37°C. Hippocampal neurons were dissected and dissociated from E18 rat embryos (Hsd:Sprague Dawley® SD®) and resuspended in Neurobasal media (Life Technologies) with PSG, then plated on Poly-L-Lysine (PLL) (Sigma Aldrich) and Laminin (Life Technologies)-coated plate. The media was changed to Neurobasal media supplemented with B27 supplement (Life Technologies) and PSG after two hours of incubation.

Seahorse assay

C2C12 cells were plated the night before at differing densities of 2,000 cells/well, 5,000 cells/well, 7,000 cells/well, 10,000 cells/well, 15,000 cells/well, and 20,000 cells/well in a Seahorse 96-well V3 microplate (Seahorse Bioscience). HEK293T cells were plated at 5,000cells/well, 10,000cells/well, 15,000cells/well, 20,000cells/well, and 25,000cells/well. Hippocampal neurons were plated 7-10 days before at differing densities of 50,000 cells/well and 100,000 cells/well. C2C12 and HEK293T cells were plated using DMEM supplemented with 10% heat inactivated FBS, 1% penicillin-

streptomycin and 2mM glutamine and maintained in an incubator with humidified 5% CO₂ at 37°C.

Media was changed the next day to XF Base Medium (Agilent Technologies, La Jolla, CA) supplemented with 1mM sodium pyruvate (Corning Cellgro Manassas, VA), and 1mM L-glutamine (Thermo Fisher Scientific, San Diego, CA). Cells were placed in an incubator without CO₂ at 37°C for 1 h prior to running the assay. The microplate was then placed into the Seahorse XFe96 Extracellular Flux analyzer (Seahorse Bioscience) to perform the Seahorse XF Cell Energy Phenotype test (Seahorse Bioscience). 1uM oligomycin and 1uM FCCP were simultaneously injected in the same port of each well after 20 min of incubation. Control wells were filled with regular DMEM used for plating cells and washed with new media the day of the assay as well. Injections were not administered to control wells.

Staining and fixing

Cells stained with dye prior to running the assay were stained with NucBlue™ Live Cell Stain (Thermo Fisher Scientific, San Diego, CA), placed in a humidified 5% CO₂ incubator at 37°C for 15 min, imaged, and one last wash was performed to remove dye and old media in all wells in the microplate. Cells fixed and stained following completion of the assay were fixed with 4% paraformaldehyde (Electron Microscopy Sciences, Hatfield, PA). Cells were fixed for 10 min, washes with 1X PBS (phosphate buffered saline) (Genesee Scientific, San Diego, CA) were

performed three times to remove PFA, and then stained with NucBlue™ Live Cell Stain (Thermo Fisher Scientific, San Diego, CA).

Cells equilibrated with dye in a non-CO₂ incubator at 37°C for fifteen minutes and media was then changed again to remove dye and any remaining old media. Cells were quickly imaged, then further incubated in a non-CO₂ incubator at 37°C prior to running the assay. Another staining procedure involved staining cells right upon completion of the assay. Nuclei dye was added within one minute of completion of the assay and allowed to incubate for fifteen minutes before imaging. Alternatively, another staining procedure required fixing cells for fifteen minutes immediately upon completion of the assay, washing three times with 1X PBS, and then staining with nuclei dye for fifteen minutes prior to imaging. These different conditions were tested on the same microplate run in the same assay.

Image Acquisition

4X and 10X images were acquired for C2C12 cells, 40X images were acquired for HEK293T cells, and 10X images were acquired for neurons using a DAPI filter on Invitrogen™ EVOS™ Digital Color Fluorescence Microscope.

Conclusion

In my master's research I found evidence of a spatial relationship between mitochondria and PFK, showed that these two have the ability to traffic together, and provided further data on how PFK is affected by O-GlcNAcylation. In doing so, we have developed further hypotheses to the nature of glycolytic flux in the brain to attempt to resolve apparently contradictory pieces of evidence. I also developed a semi-automated tool to normalize metabolic flux data through cell counting. SHCellAnalyzer is used in our lab as the standard means of normalizing metabolic flux data and a valuable tool to any lab seeking to perform metabolic flux assays without access to a dedicated cell counting instrument.

References

1. Pekkurnaz, G., Trinidad, J. C., Wang, X., Kong, D., & Schwarz, T. L. (2014). Glucose Regulates Mitochondrial Motility via Milton Modification by O-GlcNAc Transferase. *Cell*, *158*(1), 54–68.
2. Rangaraju, V., Calloway, N., & Ryan, T. A. (2014). Activity-driven local ATP synthesis is required for synaptic function. *Cell*, *156*(4), 825–835.
3. Jang, S., Nelson, J.C., Bend, E.G., Rodríguez-Laureano, L., Tueros, F.G., Cartagena, L., Underwood, K., Jorgensen, E.M. and Colón-Ramos, D.A., 2016. Glycolytic enzymes localize to synapses under energy stress to support synaptic function. *Neuron*, *90*(2), pp.278-291.
4. Jin, M., Fuller, G.G., Han, T., Yao, Y., Alessi, A.F., Freeberg, M.A., Roach, N.P., Moresco, J.J., Karnovsky, A., Baba, M. and Yates III, J.R., 2017. Glycolytic enzymes coalesce in G bodies under hypoxic stress. *Cell reports*, *20*(4), pp.895-908.
5. Ashrafi, G., & Ryan, T. A. (2017). Glucose metabolism in nerve terminals. *Current Opinion in Neurobiology*, *45*, 156–161.
6. Misgeld, T., & Schwarz, T. L. (2017). Mitostasis in Neurons: Maintaining Mitochondria in an Extended Cellular Architecture. *Neuron*, *96*(3), 651–666.
7. Hubley, M. J., Locke, B. R., & Moerland, T. S. (1996). The effects of temperature, pH, and magnesium on the diffusion coefficient of ATP in solutions of physiological ionic strength. *Biochimica et Biophysica Acta - General Subjects*, *1291*(2), 115–121.
8. Lin, M. Y., & Sheng, Z. H. (2015). Regulation of mitochondrial transport in neurons. *Experimental cell research*, *334*(1), 35–44.
9. Butkinaree, C., Park, K., & Hart, G. W. (2009). O-linked beta-N-acetylglucosamine (O-GlcNAc): Extensive crosstalk with phosphorylation to regulate signaling and transcription in response to nutrients and stress. *Biochimica et biophysica acta*, *1800*(2), 96–106.
10. Clara Bouché, Shanti Serdy, C. Ronald Kahn, Allison B. Goldfine, The Cellular Fate of Glucose and Its Relevance in Type 2 Diabetes, *Endocrine Reviews*, Volume 25, Issue 5, 1 October 2004, Pages 807–830
11. Yi, W., Clark, P.M., Mason, D.E., Keenan, M.C., Hill, C., Goddard, W.A., Peters, E.C., Driggers, E.M. and Hsieh-Wilson, L.C., 2012. Phosphofructokinase 1 glycosylation regulates cell growth and metabolism. *Science*, *337*(6097), pp.975-

980.

12. Webb, B. A., Dosey, A. M., Wittmann, T., Kollman, J. M., & Barber, D. L. (2017). The glycolytic enzyme phosphofructokinase-1 assembles into filaments. *J Cell Biol*, 216(8), 2305-2313.
13. Jang, S., Xuan, Z., Lagoy, R.C., Jawerth, L.M., Gonzalez, I., Singh, M., Prashad, S., Kim, H.S., Patel, A., Albrecht, D.R. and Hyman, A.A., 2019. The Glycolytic Protein Phosphofructokinase Dynamically Relocalizes into Subcellular Compartments with Liquid-like Properties in vivo. *bioRxiv*, p.636449.
14. Patra, K. C., & Hay, N. (2014). The pentose phosphate pathway and cancer. *Trends in biochemical sciences*, 39(8), 347-354.
15. Zhang, Y., Chen, K., Sloan, S.A., Bennett, M.L., Scholze, A.R., O'Keefe, S., Phatnani, H.P., Guarnieri, P., Caneda, C., Ruderisch, N. and Deng, S., 2014. An RNA-sequencing transcriptome and splicing database of glia, neurons, and vascular cells of the cerebral cortex. *Journal of Neuroscience*, 34(36), pp.11929-11947.
16. Rao, X., Duan, X., Mao, W., Li, X., Li, Z., Li, Q., Zheng, Z., Xu, H., Chen, M., Wang, P.G. and Wang, Y., 2015. O-GlcNAcylation of G6PD promotes the pentose phosphate pathway and tumor growth. *Nature communications*, 6, p.8468.
17. Otsu, N. (1979). A threshold selection method from gray-level histograms. *IEEE transactions on systems, man, and cybernetics*, 9(1), 62-66.
18. Huang, L. K., & Wang, M. J. J. (1995). Image thresholding by minimizing the measures of fuzziness. *Pattern recognition*, 28(1), 41-51.
19. Thevenaz, P., Ruttimann, U. E., & Unser, M. (1998). A pyramid approach to subpixel registration based on intensity. *IEEE transactions on image processing*, 7(1), 27-41.
20. Fosque, B.F., Sun, Y., Dana, H., Yang, C.T., Ohyama, T., Tadross, M.R., Patel, R., Zlatic, M., Kim, D.S., Ahrens, M.B. and Jayaraman, V., 2015. Labeling of active neural circuits in vivo with designed calcium integrators. *Science*, 347(6223), pp.755-760.
21. Kohnhorst, C.L., Kyoung, M., Jeon, M., Schmitt, D.L., Kennedy, E.L., Ramirez, J., Bracey, S.M., Luu, B.T., Russell, S.J. and An, S., 2017. Identification of a multienzyme complex for glucose metabolism in living cells. *Journal of Biological Chemistry*, 292(22), pp.9191-9203.